



Master Photonics for Security Reliability and Safety (PSRS)









Synergy of Surface Plasmon Polaritons and Photonic Crystals for Enhanced Emission in Biosensing Application

Master Thesis Report

Presented by Ayda Nasiri

and defended at
University Jean Monnet

3rd of September 2025

Academic Supervisor(s):

Prof. Matthieu Roussey

Dr. Tianlong Guo

Jury Committee:

Prof. Ciro D'amico

Prof. Amine Nait-Ali

Prof. Carlo Ricciardi

Prof. Arnaud Meyer

Synergy of Surface Plasmon Polaritons and Photonic Crystals for Enhanced Emission in Biosensing Application

Abstract

By coupling localised and propagating surface plasmon modes within photonic band gap effects, researchers have demonstrated enhanced fluorescence, spontaneous emission rates, and nonlinear optical responses. To enhance and direct molecular emission from up-conversion nanoparticles (UCNPs), we investigate a new strategy of coupling gold plasmonic gratings with one-dimensional photonic crystals (1D PhCs). The multilayers act as optical mirrors, suppressing unwanted transmission and boosting excitation and emission efficiency through directionality, while plasmonic effects amplify localised field in excitation. COMSOL simulations revealed optimal design for our fabricated nanophotonic device by calculating determining parameters in grating and multilayer (ML) structures and analyzing how grating periodicity, PhC thickness, and nanoparticles' location influence resonances in excitation and emission enhancement, making it a promising candidate for various spectroscopic applications, particularly in the field of biosensing.

Keywords: dielectric multilayers, surface plasmon polariton, photonic crystal, up-conversion emissions.

Preface

This thesis marks the conclusion of my journey in PSRS, a transformative experience that bridged my background in biomedical engineering with a growing passion for photonics and optical biosensing.

Back to the beginning of the journey, I would like to thank the PSRS consortium for giving me a fully-fundedticket to join this program. During the first half, I learned and developed in the field of photonics. A summer internship at VTT was a meaningful period thanks to the insightful researchers Prof. Jussi Hiltunen, and Dr. Sanna Aikio, equipping me with scientific thinking and sharpening my knowledge in optical measurements and design in biomedical application as well as research skills.

The beginning of the second half of the journey was going well when we had in-class studies to advance our knowledge in nano-photonics at PoliTo. I would like to thank you, Prof. Carlo Ricciardi for guidingfive of us at PoliTo. After three semesters, I have equipped enough knowledge and skills to speed up in my master's thesis. During my thesis at UEF, I would like to thank you, Prof. Matthieu Roussey, Dr. Tianlong Guo, and UEF colleagues for supporting me and excellent guidance to make my presence at OPD 2025, poster session possible; to find my way to the research world of photonics.

Looking back on the entire journey, I realise that it has been long and full of challenges, but deeply rewarding. Throughout this time, I have significantly developed my knowledge, experience, and skills in photonics. I am now thrilled and proud to announce that, following my graduation, I will continue as a doctoral researcher at UEF, advancing my thesis work on this cutting-edge topic to a higher level of research.

Joensuu, August 2025

Ayda Nasiri

Contents

Ab:	stract		3
Pre	face		4
List	of figu	ires	7
List	of tabl	les	9
1.	Intr	roduction	10
2.	The	eory	14
2	2.1. Upconversion (UC)		14
2	2.2. Sur	face plasmon polaritons	15
	2.2.1.	. Excitation Mechanism of SPPs	15
	2.2.2.	. Coupling to Surface plasmon polaritons	19
	*	Prism Coupling	20
	*	Grating Coupling	20
	*	Optical Fibre Coupling	21
	*	Planar Waveguide Coupling	21
	2.2.3.	. Propagation of Surface plasmon polaritons	21
2	2.3. Plas	smon-enhanced upconversion	22
2	2.4. Ph	otonic Crystals	23
3.	Me	thodology	26
3	3.1. Mo	delling	26
	3.1.1.	. Multilayer stacks and Photonic Band Gap model	26
	*	Transfer Matrix Method (TMM)	26
	*	Finite Element Method	28
	3.1.2	. Gold Grating model	30
	3.1.3.	. Decay rate model	31
3	3.2. Fab	prication	34
	3.2.1.	. Multilayer Structure Using Plasma-Enhanced ALD	34
	*	ALD Cycle Calibration Using Ellipsometry	35
	*	Substrate Cleaning and Surface Preparation	36
	*	Backside Protection with Tape Masking	36
	*	Multilayer Deposition via Plasma-Enhanced ALD	36

3.2.2. Grating structure using electron-beam lithography	37		
3.3. Transmission Measurement	40		
4. Results and discussions	41		
4.1. Multilayer's optical design and characterization	41		
4.2. Surface plasmon polariton excitation enhancement	42		
4.2.1. Gold Grating characterization	42		
❖ Grating thickness (g)	44		
4.2.2. Electric field enhancement mapping	46		
4.3. Up-conversion emission enhancement	47		
4.3.1. Directionality	48		
4.3.2. Quantum yield	49		
5. Conclusions	51		
References			
Appendix			
Appendix A. Abbreviations	59		
Statement of non-plagiarism60			
Supervisor approval 6			

List of figures

Fig. 1. Illustration of the excitation of surface plasmon polaritons (a) on the sides and beneath of grating integrated with multilayers and (b) in last work with grating structure [17]
Fig. 2 . Representation of p-polarized electromagnetic radiation incident upon a metal-dielectric interface at an incident angle $\theta 1$ and refracted at an angle $\theta 2$ [43]16
Fig. 3. Illustration of surface plasmon polaritons at metal-dielectric interface [44] 16 $$
The SPP dispersion curve derived from equation (2. 19) shows that the SPP mode is non-radiative, it lies below the light line in the dispersion diagram (Fig. 4). As a result, coupling mechanisms must be designed to overcome this barrier
Fig. 4. Dispersion relation curve, Dash line is the dispersion relation in dielectric media. Solid line is the dispersion relation of SPPs at the interface [45]19
Fig. 5. SPPs excitation with prism coupling with two different configurations (a) Kretschmann and (b) Otto [45]
Fig. 6. Illustration of grating coupling for excitation SPPs [45]21
Fig. 7. A schematic representation of all three configurations of photonic crystals. Different colors indicate different refractive index of the used materials23
Fig. 8. The schematic diagram of a multilayer system
Fig. 9. Model of a unit cell of the designed multilayer system in COMSOL Multiphysics excited with a TM-polarized plane wave from bottom (substrate). Perfectly matched layers (PMLs) are used to absorb outgoing waves and prevent artificial reflections 29
Fig. 10. Dispersion relation of (a) SiO2 and (b) TiO2 with alternating refractive index to the wavelength ranging from 400nm to 1200nm29
Fig. 11. (a) Model of the unit cell of multilayer along with the gold grating structure in air using periodic condition. (b) Model meshing
Fig. 12. Model for calculating decay rates; (a) the black arrows indicate the Poynting vectors and the red rectangle indicate the far field calculation, (b) in different dipole positions.
Fig. 13. ML-deposited on a fused silica wafer and patterned with the 3x4 matrix of grating structures
Fig. 14. (a) Fabricated 1D PhC on a 2-inch fused silica wafer. (b) Woollam VASE Spectroscopic Ellipsometer
Fig. 15. Scheme of a typical electron beam (e-beam) lithography process38
Fig. 16. Grating structure's pattern area39
Fig. 17. SEM images from (a) stacks of multilayer, (b) grating structure40
Fig. 18. The reflectance plots of the designed ML in TE and TM modes showing the wavelength range with high reflectance in PBG (vellow region) as a function of incident

angle including the UC emission wavelength of 540 nm41
Fig. 19. Multilayer's transmittance spectra from simulation and measurement results
Fig. 20. Determining parameters in the gold grating structure; as g for groove depth, w for width and dc for duty cycle
Fig. 21. Reflectance spectrum of SPPs over wavelength range of 400-1000 nm with (a) excitation from the substrate, (b) excitation from the air
Fig. 22. Total reflectance surface plot dependence on the grating thickness over the wavelength range of 400-1000 nm
Fig. 23. Total reflectance surface plot of the grating periodicity alternation over wavelength range of 700-1000 nm with (a) duty cycle of 0.8, (b) duty cycle of 0.5 showcasing the peak and dip of the SSP resonances in the reflectance spectrum with d=12
Fig. 24. (a) Total reflectance surface plot of the grating duty cycle alternation over the wavelength range of 700-1000 nm. (b) EF at excitation wavelength 976 nm with d=1230 nm
Fig. 25. The electric field cross section of the final nanostructure with the corresponding enhancement factor and SPPs at the excitation wavelength of 976 nm.
Fig. 26. The localised electric field enhancement (a) mapping of different points around the depicted grating, (b) along the determined cross section of the grating thickness.
Fig. 27. The emission directionality for dipole on a a) substrate, b) flat gold, c) multilayer structure, and d) multilayer with grating structure
Fig. 28. (a) The Poynting vector for four different structures at the emission angle 0 $^{\circ}$, (b) the upward power output flow ratio normalized to the substrate's power for a full-scattering range of the emission angle from -16.5 $^{\circ}$ to 16.5 $^{\circ}$
Fig. 29. Computational investigation of the quenching effect with a UCNP near a gold surface. (a) Illustration of the location of the UCNP on flat gold or on grating with six cases (P1, P2, P3, P4, P5, and P6). (b) The quenching effect of the UCNP on flat gold and on grating as a function of the dipole emission angle in six points. The quenching effect is evaluated by the quantum yield ratio of the UCNP near the gold surface (qp) and in free space ($q0$). The dipole emission angle is determined by the collection angle of the used objective ($\pm 16.5^{\circ}$). The quenching effect with the duty cycle changes at the locations (c) P ₄ and (d) P ₁
Fig. 30. a) The comparison chart of UC enhancement ratio showcasing the effect of adding multilayers to the grating for the emission. b) Dipole emission at the position P_4 with emission angle of -16.5° and wavelength of 540 nm

List of tables

Table 1. Indicating parameters in the ALD technique-based deposition of the ML \ldots	37
Table 2. Parameters of transmission measurements	40

1. Introduction

Most single-molecule detection technologies rely on fluorescence measurements within confined volumes. Far-field optical microscopy enables probing of attoliter (10-100 aL) volumes and has been widely used for Förster Resonance Energy Transfer (FRET)-based studies of protein folding dynamics [1]. To further enhance detection sensitivity, near-field optics particularly, plasmonics [2], have enabled probing zeptoliter (zL) volumes, significantly increasing signal enhancement. Beyond fluorescence, plasmonic techniques also allow for label-free detection of individual molecular interactions in real time. For instance, gold nanorod-based plasmon resonance enables the optical detection of single, non-absorbing molecules, advancing the study of biomolecular recognition events [3]. Recent advances in plasmonic singlemolecule detection have demonstrated remarkable sensitivity and temporal resolution. Localised surface plasmon resonance sensors based on metallic nanostructures enable detection of single molecules without fluorescent labeling, providing a powerful and real-time approach to probing dynamic biomolecular interactions [4,5]. These sensors are particularly advantageous for detecting non-fluorescent or weakly scattering molecules by monitoring local refractive index changes upon binding [6]. Furthermore, some plasmonic platforms now offer sub-microsecond temporal resolution, enabling the observation of fast, transient events in molecular recognition [7]. However, several challenges remain. High sensitivity in plasmonic systems often comes at the cost of complex nanostructure fabrication and surface functionalization, which are critical for achieving specificity and reducing non-specific binding [8]. In addition, plasmonic sensors are inherently sensitive to environmental conditions, such as temperature and bulk refractive index fluctuations, which can impact measurement stability and reproducibility [6]. Despite these limitations, plasmonic approaches continue to push the boundaries of optical detection, offering new possibilities in single-molecule biophysics.

In addition to conventional fluorescence-based techniques, upconversion luminescence (UCL) has emerged as a promising alternative for single-molecule detection. UCL involves the sequential absorption of two or more low-energy photons, leading to the emission of a higher-energy photon. This anti-Stokes emission mechanism offers several advantages over traditional fluorescence, including reduced background autofluorescence, deeper tissue penetration due to near-infrared excitation, and improved photostability. Lanthanide-doped UCNPs, such as NaYF₄:Yb³⁺/Er³⁺, have been widely studied for their efficient UCL properties and potential in bioimaging applications [9-11]. Despite the benefits of UCL, lanthanide-doped UCNPs often exhibit low quantum yields due to concentration and surface quenching effects, which significantly reduce emission efficiency, especially in smaller particles [12-15]. Coating UCNPs with inert shells can help mitigate these losses, but challenges in optimizing luminescence remain. To address this, researchers have explored

the enhancement of UCL through coupling with surface plasmon polaritons (SPPs) in the surface plasmon-coupled emission (SPCE) platform. SPPs are collective oscillations of electrons at the interface between a metal and a dielectric, which can amplify the local electromagnetic field and, consequently, the UCL intensity. In a notable study, Das et al. reported a remarkable ~1000fold enhancement in UCL intensity using lithographically fabricated metalinsulator-metal (MIM) nanostructures [16]. These nanostructures were carefully engineered to match the plasmonic resonance with the excitation wavelength of lanthanide-doped UCNPs, resulting in highly confined electromagnetic fields and efficient coupling. Additionally, the structures were designed to be water-dispersible, supporting potential biomedical applications. In contrast, Le et al. demonstrated a more accessible enhancement approach using gold gratings to excite SPPs, achieving up to a 65fold increase in UCL intensity at low excitation powers [17]. Their design emphasized spectral tuning and local field amplification via SPPs, offering a scalable and power-efficient solution. While the MIM-based system yields a significantly higher enhancement, it involves more complex fabrication and integration. On the other hand, the grating-based method offers simpler implementation and tunability, making it attractive for applications where moderate enhancement and low power operation are desirable.

While SPCE platforms have enabled highly sensitive biosensing, their performance is fundamentally limited by significant ohmic losses in metalbased structures. These losses restrict the efficiency and range of SPPs, especially in active sensing or light-emitting applications. To overcome these limitations, photonic crystal-based architectures, particularly 1D PhCs, have been explored as complementary or alternative platforms to support low-loss surface-bound modes. In contrast to SPCE, where field enhancement arises from SPPs, 1D PhCs can support Bloch surface waves (BSWs) and internal optical modes (IOMs), which offer high Q-factors, reduced losses, and extended propagation lengths [18,19]. The integration of surface plasmon polaritons and photonic crystal structures represents a novel approach to enhancing light emission in nanophotonic devices. This hybrid mechanism capitalizes on the strong field confinement of SPPs and the wavelengthselective feedback provided by PhC, leading to significant improvements in emission efficiency, directionality, and spectral purity [20], as shown by Bhaskar et al., who combined silver nanowire SPPs with photonic crystalcoupled emission (PCCE) to enable single-molecule cholesterol detection with improved sensitivity and directional emission control [21]. By coupling and propagating localised surface plasmon modes with photonic band gap effects, researchers have demonstrated enhanced fluorescence, spontaneous emission rates, and nonlinear optical responses [22]. For instance, Paternò et al. fabricated a one-dimensional hybrid plasmonic-photonic crystal by depositing a silver layer on a PhC substrate, enabling the detection of E. coli through analyte-induced shifts in photonic resonances, demonstrating both spectral tunability and label-free detection capability [23]. Liu et al. introduced a nanoantenna-microcavity hybrid by coupling plasmonic gold nanorods with dielectric photonic crystal slabs, achieving highly localized electromagnetic field enhancement suitable for probing weak light and matter interactions at single-molecule sensitivity levels [24]. In another design, Hajshahvaladi et al. embedded metallic rods within a photonic crystal lattice, creating a hybrid refractive index sensor that achieved an exceptional figure of merit of 2388 RIU⁻¹ and sensitivity of 1672 nm/RIU, demonstrating superior performance compared to purely plasmonic or photonic systems [25]. Krupin and Berini engineered a long-range SPP waveguide integrated with a photonic crystal, achieving the sensitive and specific detection of cardiac troponin I, with implications for early cardiovascular diagnostics [26]. Similarly, Boltasseva et al. demonstrated the effective propagation of long-range SPPs through photonic crystal environments, showing that PhC structures can control and guide SPPs over extended distances, crucial for integrated biosensing platforms [27]. Rifat et al. developed a photonic crystal fiber (PCF) biosensor based on surface plasmon resonance (SPR), where the fiber structure was coated with a thin gold layer to excite SPPs. Their device offered practical implementation benefits such as high sensitivity, compactness, and ease of integration into portable sensing systems [28]. Hall et al. presented a dual-structured plasmonic-photonic crystal biosensor that combined PhC structures with plasmonic nanostructures to achieve tunable, high-Q resonances. Their system demonstrated enhanced detection of biomolecular binding events due to improved light confinement and surface sensitivity, showcasing the value of hybrid integration for precision biosensing [29].

In our work (Fig. 1 (a)), we design and investigate gold (Au) plasmonic gratings integrated with 1D PhC to enhance molecular emission in a preferential direction. The Au gratings provide strong plasmonic enhancement via SPPs, while the 1D PhC facilitates excitation and suppresses unwanted transmission at the molecule signal wavelengths. This synergy enhances emission intensity and improves sensitivity in spectroscopic applications more in comparison with the approach used in the work of Le *et al.* without MLs (Fig. 1 (b)). Our study covers theoretical and experimental aspects, analyzing grating periodicity, PhC thickness, nanoparticles' location and their influences on SPP resonance and field enhancement. Through numerical simulations of finite element method (FEM), we identify optimal configurations for emission control on directionality and quenching effect. Additionally, we outline feasible fabrication strategies for precise structural realization, paving the way for next generation nanophotonic devices.



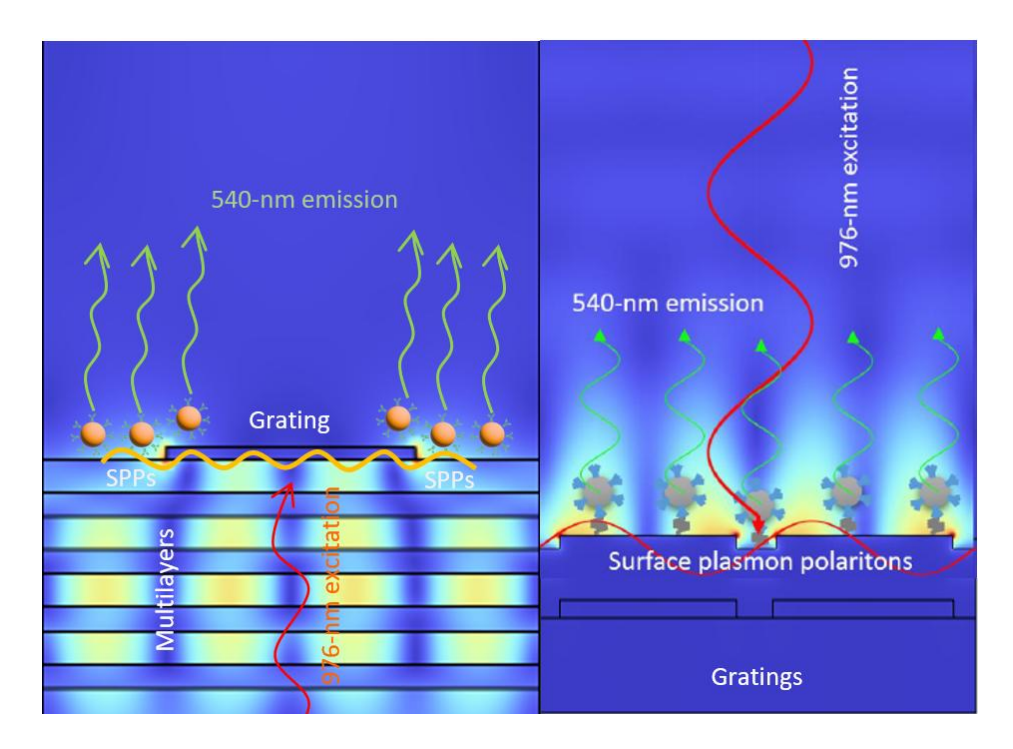


Fig. 1. Illustration of the excitation of surface plasmon polaritons (a) on the sides and beneath of grating integrated with multilayers and (b) in last work with grating structure [17].

By providing a comprehensive understanding of this hybrid platform, we establish a foundation for its application in high sensitivity biosensing, fluorescence enhancement, and quantum optics.

2. Theory

2.1. Upconversion (UC)

UCL is a unique nonlinear optical phenomenon in which the sequential absorption of two or more photons of lower energy or longer wavelength results in the emission of a single photon of higher energy or shorter wavelength [12,30]. This process contrasts with conventional fluorescence, where a single high-energy photon is absorbed and re-emitted at a lower energy. Due to its anti-Stokes emission behavior, UC has garnered increasing attention for applications in biomedical imaging, biosensing, photovoltaics, security printing, and display technologies [31,32].

One of the major advantages of UCL, especially in biological and sensing applications, lies in its ability to minimize background signals such as autofluorescence and scattering, which are prevalent under ultraviolet (UV) or visible excitation [33]. Since UC processes are typically excited using near-infrared (NIR) light (e.g., 980 nm or 808 nm), they offer deep tissue penetration, low photodamage, and high signal-to-noise ratios, making them highly suitable for in vivo applications and sensitive detection platforms [34,35].

In UCNPs, the luminescent properties primarily arise from carefully selected lanthanide dopant ions embedded within a crystalline host lattice, which are the most widely studied UC materials. These are typically composed of an inert host lattice (e.g., NaYF₄, NaGdF₄) that accommodates optically active lanthanide ions such as ytterbium (Yb³+), erbium (Er³+), or thulium (Tm³+). Lanthanide ions possess a ladder-like arrangement of energy levels, which are shielded from the surrounding lattice vibrations by the outer 5s and 5p electrons. This leads to sharp emission bands, long excited-state lifetimes, and well-defined photon energy conversion pathways.

Sensitizer ions, such as Yb³+ or neodymium (Nd³+), are chosen for their strong absorption in the NIR region and serve to absorb excitation photons efficiently. The absorbed energy is then non-radiatively transferred to activator ions like Er^{3+} , Tm^{3+} , or holmium (Ho³+), which emit higher-energy photons through radiative transitions. The host material, typically a low-phonon energy fluoride matrix such as sodium yttrium fluoride (NaYF₄), plays a crucial role in minimizing non-radiative losses and providing a stable environment for efficient energy transfer between ions. Among these, β -NaYF₄ is widely regarded as the most efficient host due to its favorable crystal field and low vibrational energy, which suppress multiphonon relaxation processes and enhance UC efficiency [31,32].

Lanthanide-doped UCNPs exhibit several mechanisms of UC, including excited state absorption (ESA), energy transfer upconversion (ETU), and photon avalanche (PA). In ESA, a single ion sequentially absorbs multiple photons via intermediate metastable states, emitting higher-energy photons upon relaxation. ETU, the most widely used and efficient UC mechanism,

involves energy transfer from sensitizer ions to activators enabling multiphoton excitation through energy migration and accumulation. In contrast, PA is a nonlinear and rare mechanism where an initial excitation leads to a positive feedback loop of energy transfer and absorption, resulting in intense emission bursts.

Despite their potential, UCNPs often suffer from low quantum efficiency under low-power continuous-wave (CW) excitation. This is largely due to the intrinsically low absorption cross-sections of lanthanide ions $(10^{-20}-10^{-22}~\text{cm}^2)$ [12], especially for activators like Er^{3+} and Tm^{3+} . While Yb^{3+} is commonly used to enhance absorption, the efficiency of energy transfer remains reliant on spectral overlap and spatial proximity [32]. High dopant concentrations may cause concentration quenching and cross-relaxation, limiting emission above $^2-3$ mol% in NaYF₄ hosts [35, 36]. Surface-related nonradiative losses due to defects, -OH groups, or phonons further reduce emission, though passivation shells can help [38]. Additionally, back energy transfer from activators to sensitizers, especially in systems like $\text{Yb}^{3+}/\text{Er}^{3+}$, can alter emission color and reduce overall output [38]. Finally, thermal effects, structural degradation, and light scattering in complex environments also contribute to UC efficiency loss and long-term instability [39, 40].

2.2. Surface plasmon polaritons

SPPs are electromagnetic surface waves that propagate along the boundary between a dielectric and a metal. These waves are tightly bound to the interface due to the coupling between the incident electromagnetic field and the collective oscillations of free electrons, commonly referred to as surface charges on the metal surface [41]. The surface plasma oscillations are accompanied by a mixed transversal and longitudinal electromagnetic fields where the transversal field evanescently decays in the perpendicular direction [42].

2.2.1. Excitation Mechanism of SPPs

To initiate these oscillations, one must use light that is p-polarized (transverse magnetic or TM mode), where the electric field vector lies in the plane of incidence. Consider a p-polarized light wave incident on a flat metal-dielectric interface at an angle θ_1 (Fig. 2). The light traveling in the dielectric medium has a wavevector $k_d = \frac{2\pi n_d}{\lambda}$, where n_d is the refractive index of the dielectric and λ is the wavelength of the light in vacuum. When the light strikes the interface, part of it is reflected, maintaining the same angle θ_1 due to momentum conservation along the interface. Meanwhile, the transmitted component continues into the metal with a new angle θ_2 and a wavevector $k_m = \frac{2\pi n_m}{\lambda}$, where n_m is the metal's refractive index. Conservation of the wavevector's component parallel to the interface leads to the relation:

$$k_{d,x} = k_{m,x} \quad \text{or} \quad n_d \sin \theta_1 = n_m \sin \theta_2, \tag{2.1}$$

which is Snell's law.

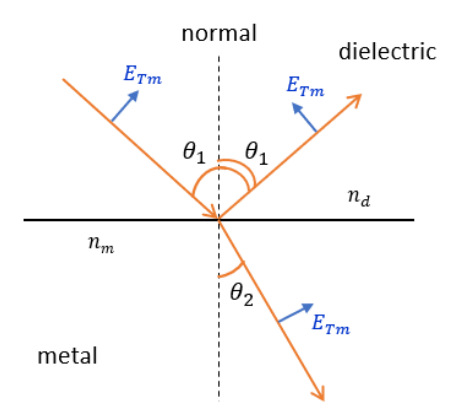


Fig. 2 . Representation of p-polarized electromagnetic radiation incident upon a metal-dielectric interface at an incident angle θ_1 and refracted at an angle θ_2 [43].

At optical frequencies, metals like gold, silver, or copper typically exhibit a smaller refractive index (or more accurately, a complex permittivity with negative real part) than dielectrics. Because $n_d > n_m$, a critical angle θ_c exists, beyond which no light can propagate into the metal in the traditional sense. This critical angle is given by:

$$\sin\theta_c = \frac{n_m}{n_d} \tag{2.2}$$

For incident angles greater than θ_c , total internal reflection occurs, and instead of transmission, an evanescent field is generated that decays exponentially into both media. This non-propagating field can interact with the surface charges and give rise to SPPs.

The interaction between the oscillating electric field of the p-polarized light and the conduction electrons in the metal induces a time-varying polarization at the interface, which manifests as surface charge oscillations. These oscillations, in turn, generate electromagnetic fields that are confined to and decay perpendicularly away from the interface, features characteristic of SPPs (Fig. 3).

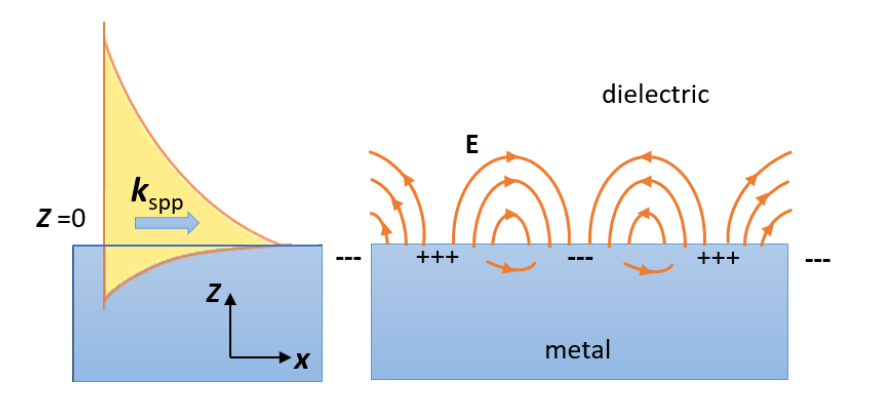


Fig. 3. Illustration of surface plasmon polaritons at metal-dielectric interface [44].

Importantly, the electric field component parallel to the interface (E_x) is

continuous across the boundary due to the absence of free surface charges. However, the perpendicular component (E_z) may be discontinuous because it is related to the displacement field $D_z = \varepsilon \varepsilon_0 E_z$, which must remain continuous across the interface in the absence of free charges. The difference in permittivity ε across the boundary necessitates a change in E_z , resulting in a surface polarization that plays a key role in SPP excitation.

It is essential to highlight that s-polarized (transverse magnetic or TE mode) light, where the electric field is perpendicular to the plane of incidence, does not contribute to the generation of surface charge oscillations, as it lacks a normal electric field component at the interface. Therefore, only p-polarized waves are effective in exciting SPPs.

These waves must obey Maxwell's equations in both media to accurately describe their spatial behavior and field distributions. To analyze SPP propagation mathematically, consider a simplified model in which the interface lies in the x-y plane, and the wave propagates along the x-direction.

For the dielectric region (above the interface, i.e., z > 0), the electric and magnetic fields (E, H) of the SPPs can be written as:

$$E_d = (E_{x,d}, 0, E_{z,d})e^{-k_{z,d}z}e^{i(k_x x - \omega t)}$$
(2.3)

$$H_d = (0, H_{y,d}, 0)e^{-k_{z,d}z}e^{i(k_x x - \omega t)}$$
(2.4)

Similarly, for the metallic region (below the interface, i.e., z < 0), the fields are:

$$E_m = (E_{x,m}, 0, E_{z,m})e^{-k_{z,m}z}e^{i(k_x x - \omega t)}$$
(2.5)

$$H_m = (0, H_{y,m}, 0)e^{-k_{z,m}z}e^{i(k_x x - \omega t)}$$
(2.6)

Here, k_{χ} represents the component of the wavevector along the propagation direction, while $k_{z,d}$ and $k_{z,m}$ are the decay constants in the dielectric and metal, respectively. These decay constants ensure that the fields are evanescent in the z-direction, which is characteristic of SPPs.

To determine the relations between the electric field components, we use the divergence condition for the electric field from Maxwell's equations:

$$\nabla \cdot \mathbf{E} = 0 \tag{2.7}$$

Applying this to the fields in each medium yields;

$$E_{z,d} = i \frac{k_x}{k_{z,d}} E_{x,d} \tag{2.8}$$

$$E_{z,d} = i \frac{k_x}{k_{z,d}} E_{x,d}$$

$$E_{z,m} = i \frac{k_x}{k_{z,m}} E_{x,m}$$
(2. 8)

Additionally, the curl equation from Maxwell's laws:

$$\nabla \times \mathbf{E} = -\frac{1}{c} \frac{\partial \mathbf{H}}{\partial t} \tag{2.10}$$

can be used to derive the magnetic field in terms of the electric field. For the dielectric and metallic region, this gives:

$$-k_{z,d}E_{z,d} - ik_x E_{z,d} = ik_0 H_{y,d}$$
 (2.11)

$$k_{z,m}E_{z,m} - ik_x E_{z,m} = ik_0 H_{y,m}$$
 (2.12)

Where $k_0 = \frac{\omega}{c}$ is the free-space wave number. These equations further couple the electric and magnetic fields, ensuring that the electromagnetic boundary conditions are satisfied at the interface.

In terms of equations (2. 8) and (2. 9), equations (2. 11) and (2. 12) can be

expressed as follows, respectively:

$$-\varepsilon_d k_0 E_{x,d} = i k_{z,d} H_{v,d} \tag{2.13}$$

$$\varepsilon_m k_0 E_{x,m} = -i k_{z,m} H_{y,m} \tag{2.14}$$

Next, the dispersion properties of the fields follow from the wave equation in each material. For SPPs, the components of the wavevector in the z-direction satisfy:

$$k_{z,d}^2 = k_x^2 - \varepsilon_d k_0^2 \tag{2.15}$$

$$k_{z,m}^2 = k_x^2 - \varepsilon_m k_0^2 \tag{2.16}$$

These equations describe the evanescent nature of the fields perpendicular to the interface. Notably, for SPPs to exist, $k_{z,d}$ and $k_{z,m}$ must be real and positive, which implies that the in-plane wavevector k_x exceeds the wave number in both media.

Applying boundary conditions at the metal-dielectric interface (z=0), the continuity of the tangential components of electric and magnetic fields yields; $E_{x,d}=E_{x,m}$, $H_{y,d}=H_{y,m}$. Combining equations (2. 13) and (2. 14), and using these boundary conditions, we obtain:

$$\frac{k_{\rm z,d}}{k_{\rm z,m}} = -\frac{\varepsilon_{\rm d}}{\varepsilon_{\rm m}} \tag{2.17}$$

This equation ensures energy conservation across the interface and reflects the discontinuity in the normal component of the electric field due to differing permittivities.

To derive the SPP dispersion relation, we insert expressions (2. 15) and (2. 16) into (2. 17), and solve for the propagation constant k_x . The result is:

$$k_{\chi} = k_0 \sqrt{\frac{\varepsilon_{\rm d} \, \varepsilon_{\rm m}}{\varepsilon_{\rm d} + \varepsilon_{\rm m}}} \tag{2.18}$$

This expression, typically denoted as k_{spp} , defines the wavevector of the surface plasmon polariton mode:

$$k_{spp} = k_0 \sqrt{\frac{\varepsilon_{\rm d} \, \varepsilon_{\rm m}}{\varepsilon_{\rm d} + \varepsilon_{\rm m}}} \tag{2.19}$$

The key feature of this dispersion relation is that $k_{SPP} > k_0$, meaning the momentum of the SPP ($\hbar k_{SPP}$) is larger than that of a photon in free space at the same frequency. This mismatch prevents direct excitation of SPPs by light unless additional momentum is provided, such as through a prism (Kretschmann or Otto configuration) or a grating.

The resonance condition for strong coupling occurs when the denominator approaches zero; $\epsilon_d + \epsilon_m = 0.$ This resonance criterion highlights that SPP excitation is highly sensitive to the permittivities of the metal and dielectric, enabling applications in surface sensing and biosensing due to changes in ϵ_d . The SPP dispersion curve derived from equation (2. 19) shows that the SPP mode is non-radiative, it lies below the light line in the dispersion diagram (Fig. 4). As a result, coupling mechanisms must be designed to overcome this barrier.

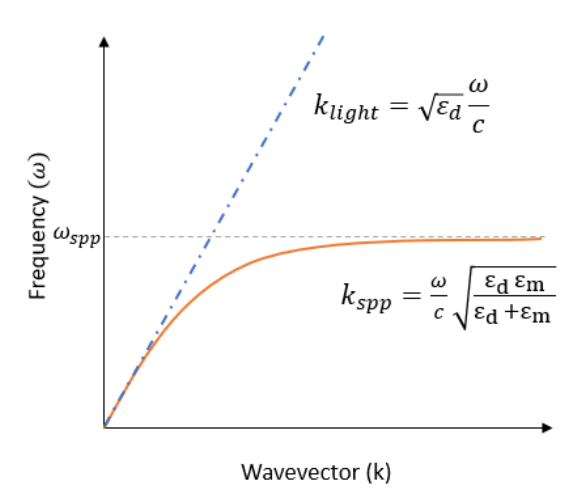


Fig. 4. Dispersion relation curve, Dash line is the dispersion relation in dielectric media. Solid line is the dispersion relation of SPPs at the interface [45].

The dielectric function of a metal can be approximated by the Drude model:

$$\varepsilon_{\rm m}(\omega) = 1 - \frac{\omega_p^2}{\omega^2} \tag{2.20}$$

where ω_p is the plasma frequency of the metal. Using this in the dispersion or resonance condition, the frequency of the SPP becomes:

$$\omega_{spp} = \frac{\omega_p}{\sqrt{1+\varepsilon_d}} \tag{2.21}$$

This implies that the SPP frequency is always less than the plasma frequency of the metal and depends on the dielectric environment. SPP fields decay exponentially away from the interface into both media. The penetration depths into the dielectric and the metal, denoted as δ_d and δ_m respectively, are defined as $\delta_d = \frac{1}{k_{z,d}}$ and $\delta_m = \frac{1}{k_{z,m}}$, representing the distances over which the electric fields decay to 1/e of their initial values. Substituting equations (2. 18) and (2. 19), the characteristic penetration depths can be defined as:

$$\delta_{\rm d} = \frac{1}{k} \left(\frac{\varepsilon_{\rm d} + \varepsilon_{\rm m}}{-\varepsilon_{\rm d}^2} \right)^{1/2} \tag{2.22}$$

$$\delta_{\rm m} = \frac{1}{k} \left(\frac{\varepsilon_{\rm d} + \varepsilon_{\rm m}}{-\varepsilon_{\rm m}^2} \right)^{1/2} \tag{2.23}$$

2.2.2. Coupling to Surface plasmon polaritons

Due to the dispersion characteristics of SPPs, the in-plane momentum of an SPP exceeds that of a free-space photon at the same frequency. According to the Eq. (2. 19) and Fig. 4, there is a momentum mismatch between free-space light and SPPs. To overcome this, specialized coupling configurations are employed to facilitate energy transfer from the incident light to the SPP mode by matching their momenta.

Prism Coupling

As shown in Fig. 5, this configuration is employed by two different methods that are described below.

- Kretschmann Configuration: one of the most widely used methods for exciting SPPs is the Kretschmann configuration, in which a thin metal film is deposited on the base of a dielectric prism. The incident light enters the prism at an angle greater than the critical angle for total internal reflection. This increases the in-plane component of the light's wavevector. When this component matches the SPP wavevector at the metal-air interface, resonant tunneling occurs, and energy is coupled into the SPP mode. The efficiency of this coupling strongly depends on the thickness of the metal film; too thick a film suppresses tunneling, while too thin a film increases optical losses.
- Otto Configuration: In cases where direct contact between the prism and metal film is not possible or desirable, the Otto configuration is used. Here, a small air gap is maintained between the prism and the metal surface. When the incident light undergoes total internal reflection inside the prism, an evanescent field extends through the gap. If the gap is thin enough, this evanescent wave can excite SPPs at the metal-air interface.

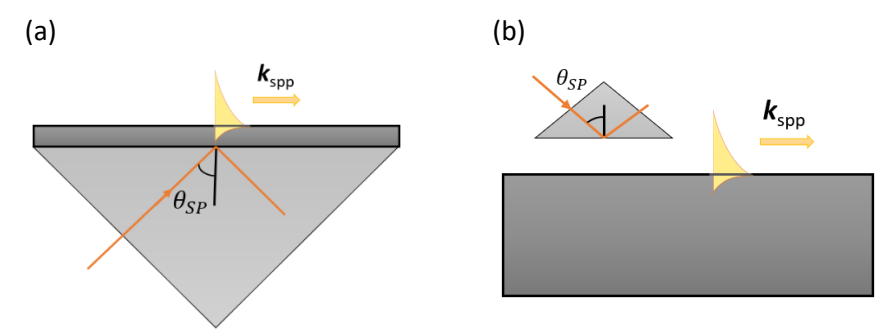


Fig. 5. SPPs excitation with prism coupling with two different configurations (a) Kretschmann and (b) Otto [45].

Grating Coupling

Another effective method to match the momentum of photons and SPPs involves using a diffraction grating on the metal surface (Fig. 6). The periodic corrugations on the surface scatter incident light, generating diffracted modes with additional momentum. If the in-plane component of a diffracted order satisfies the SPP dispersion relation, coupling occurs:

$$k_{spp} = k_0 \sin \theta \pm m \frac{2\pi}{\Lambda} \tag{2.24}$$

where m is the diffraction order and Λ is the grating period. This method provides wavelength- and angle-tunable excitation, and is useful in integrated plasmonic devices.

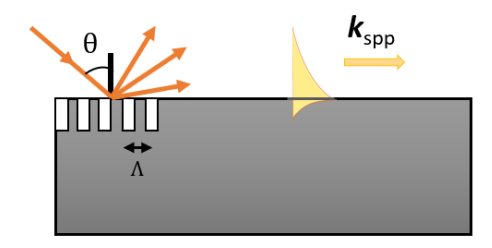


Fig. 6. Illustration of grating coupling for excitation SPPs [45].

Optical Fibre Coupling

Optical fibres provide a miniaturized and flexible platform for SPP excitation. The cladding of the fibre is removed in a section and replaced with a thin metal coating that interfaces with a sensing medium. The evanescent field of guided light in the core extends into the metal layer and, under phase-matching conditions, can excite SPPs at the outer interface.

Coupling efficiency depends on multiple parameters including fibre geometry, core diameter, wavelength, and the mode structure. Notably, tapered fibres offer stronger field confinement and deeper evanescent penetration, making them especially effective for SPP excitation compared to standard straight fibres.

Planar Waveguide Coupling

SPPs can also be excited using integrated optical waveguides. In this configuration, light propagates in a dielectric slab or channel waveguide with a thin metal overlay. If the effective index of the guided mode matches that of the SPP, the guided light can evanescently couple into the SPP mode on the outer metal interface. This is conceptually similar to the Kretschmann configuration, with the waveguide replacing the prism.

Waveguide coupling is especially suitable for on-chip plasmonic circuits and sensors, as it allows compact integration with photonic components.

2.2.3. Propagation of Surface plasmon polaritons

Once light is coupled into a SPP mode at a flat metal—dielectric interface, the SPP propagates along the interface. However, this propagation is subject to attenuation due to intrinsic material losses, primarily ohmic losses in the metal, which stem from the interaction between the oscillating surface charges and the metal's conduction electrons.

The extent to which an SPP can propagate before its amplitude significantly diminishes is characterized by its propagation length. This is defined as the distance along the interface at which the intensity of the SPP decays to 1/e of its original value. The attenuation is governed by the imaginary part of the complex SPP wavevector; $k_{spp} = k_{spp,r} + k_{spp,i}$, where $k_{spp,r}$ is the real part (associated with phase propagation), and $k_{spp,i}$ is the imaginary part (associated with damping). Based on the SPP dispersion relation (Eq. (2. 19)),

the propagation length δ_{spp} can be expressed as:

$$\delta_{spp} = \frac{1}{2k_{spp,i}} = \frac{\lambda}{2\pi} \left(\frac{\varepsilon_{m,r} + \varepsilon_d}{-\varepsilon_{m,r} \, \varepsilon_d} \right)^{3/2} \, \frac{\varepsilon_{m,r}^2}{\varepsilon_{m,i}} \tag{2.25}$$

Where λ is the free-space wavelength of the incident light, $\epsilon_{m,r}$ and $\epsilon_{m,i}$ are the real and imaginary components of the metal's complex dielectric function, $\epsilon_m = \epsilon_{m,r} + i\epsilon_{m,i}$, and ϵ_d is the dielectric constant of the adjoining dielectric medium

This equation indicates that the propagation length of an SPP is strongly influenced by both the material properties of the metal and the operating wavelength [46].

2.3. Plasmon-enhanced upconversion

The dominant UC mechanism is ETU, where Yb³+ ions absorb near-infrared photons and transfer energy to Er³+ ions, resulting in green emission. The green UC emission depends on excitation intensity: under weak excitation, it follows a two-photon process, with emission rate proportional to the square of the excitation rate; under strong excitation, the emission rate becomes linearly proportional to the excitation rate due to saturation of intermediate energy levels. Thus, UC emission can be enhanced by increasing either the excitation efficiency (via stronger local electric fields) or the emission efficiency (via improved quantum yield).

The UC enhancement can be expressed as [47];

$$F_E = F_{exc} \cdot F_{em} \tag{2.26}$$

Here, F_{exc} and F_{em} represent the excitation and emission enhancements, respectively. Since these processes are incoherent, they are treated independently.

In strong excitation, the intermediate states saturate, and the process behaves more linearly, scaling with the square of the local field;

$$F_{exc} \alpha \frac{|\mathbf{E}_{p}|^{2}}{|\mathbf{E}_{0}|^{2}} \tag{2.27}$$

The intrinsic quantum yield of UCNPs in free space is defined as the ratio of radiative transitions to total decay rates, $q_0=\Upsilon^0_r/\ (\Upsilon^0_r+\Upsilon^0_{nr})$, where Υ^0_r and Υ^0_{nr} are intrinsic radiative and nonradiative decay rates, respectively and unchanged in the environment. When UCNPs are placed near a plasmonic structure, the quantum yield becomes $q_p=\Upsilon^p_r/\ (\Upsilon^0_r+\Upsilon^0_{nr}+\Upsilon^p_{abs})$, where Υ^p_r and Υ^p_{abs} are the additional radiative decay rate and absorption loss due to the plasmonic environment. The quantum yield enhancement can be expressed as:

$$q_p = \frac{\gamma_r^p / \gamma_r^0}{\frac{\gamma_r^p + \frac{abs}{r_r^0} + (1 - q_0)/q_0}{\gamma_r^0}}$$
(2.28)

The emission enhancement factor is then calculated as $F_{em}={\rm q}_p/{\rm q}_0$, indicating that UCNPs with inherently low ${\rm q}_0$ benefit more from plasmonic emission enhancement.

2.4. Photonic Crystals

Over the past five decades, semiconductors have significantly transformed modern life, primarily due to major advancements in electronics. These advancements are fundamentally driven by the movement of electrons within a periodic atomic lattice, known as the crystal lattice which influences how electrons and electromagnetic waves move through the material. In solid-state physics, only electrons with specific energies and momenta can move freely, while others are blocked by energy band gaps, regions where no electron states exist. The interaction of electrons with the periodic arrangement of atoms in solids leads to the development of energy bands, which underpin numerous technological applications [48].

A PhC mirrors this concept in optics. Instead of atoms, it features a periodic arrangement of materials with different dielectric constants (or refractive indices) in one, two, or all three spatial dimensions. This periodic variation in the refractive index affects how light propagates, creating photonic band gaps (PBGs), frequency ranges where light cannot travel through the crystal in certain directions. These structures can occur naturally, such as in butterfly wings, or be engineered for applications in waveguides, optical fibers, sensors, and lasers. Based on the periodicity of dielectric material in one or more axes, they are categorized as one-dimensional (1D), two-dimensional (2D), or threedimensional (3D) photonic crystals (Fig. 7). The 1D variants, also referred to as multilayers' structures, have been thoroughly researched and documented [49–51]. They are composed of alternating layers of two materials with distinct refractive indices, causing a periodic variation along one direction while the other two remain uniform. In 2D photonic crystals, the refractive index varies along two directions but remains constant along the third [52-54]. In contrast, 3D photonic crystals involve a periodicity of the refractive index in all three dimensions [55–57].

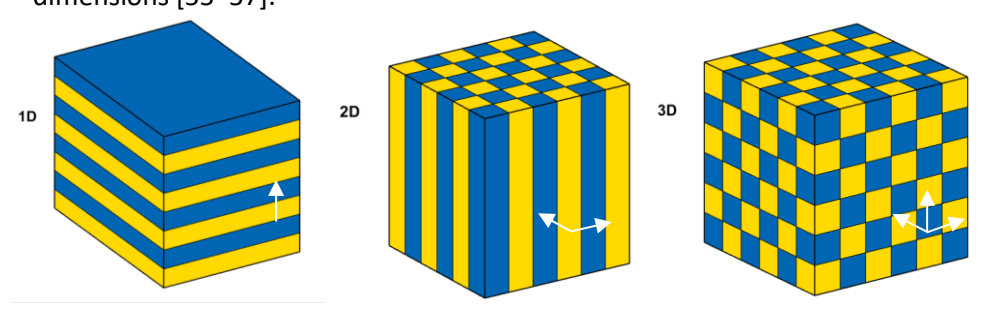


Fig. 7. A schematic representation of all three configurations of photonic crystals. Different colors indicate different refractive index of the used materials.

Electron waves are scalar-valued functions and follow the Schrödinger equation, whereas electromagnetic wave functions are vectorial and governed by Maxwell's equations. Furthermore, electron wavelengths are significantly shorter than those of photons, meaning that atomic-scale periodicities, which strongly affect electrons, appear uniform to visible light. To influence light, the periodic structures must have lattice constants on the order of several hundred nanometers, since Maxwell's equations in such media form an eigenvalue

problem analogous to the Schrödinger equation and effectively making photonic crystals behave like periodic structures in solid-state physics [58].

When light strikes a periodic structure, it is reflected at each interface. Under certain conditions, these reflected waves can constructively interfere, satisfying a version of Bragg's condition adapted for photonic structures [48]:

$$m \lambda = 2n_{eff}d \tag{2.29}$$

where m is the diffraction order, λ is the wavelength of the reflected light, n_{eff} is the effective refractive index of the periodic medium, and d is the periodicity (lattice constant) in the direction of light propagation. When this condition is fulfilled, strong reflection occurs at that specific wavelength.

When light is incident on a photonic crystal structure, certain wavelengths of the incoming light are reflected based on Eq. (2. 29), which depends on the periodicity of the structure and its effective refractive index. This results in a peak in reflection and a corresponding dip in transmission at a specific wavelength, known as the photonic stopband or pseudobandgap wavelength. If this stopband appears for all directions of light propagation and for both polarization states, it is referred to as a complete photonic bandgap [58]. Importantly, the wavelengths blocked from transmission are not absorbed by the structure. In contrast to semiconductors, where the bandgap corresponds to light absorption, the bandgap in a photonic crystal refers to a range of wavelengths that cannot propagate through the structure, leading to strong reflection instead of absorption.

Energy bands both allowed and forbidden ones can emerge interesting optical properties of photonic crystals [59]. As a result, the dispersion relation, which defines the band structure, provides valuable insight into many of the optical behaviors seen in these materials.

As for the periodic structures in a lattice, the Bloch theorem is also applicable for photonic crystals and is given by [59]:

$$H(r) = U_{kn}(r)e^{ikr}$$
 (2.30)

Where $U_{kn}(r)$ is a periodic function matching the lattice periodicity, and k is the wavevector within the first Brillouin zone.

Owing to the lattice's translational symmetry, solutions can be restricted to this zone, with each band identified by an integer n [60]. A widely used approach to solve Eq. (2. 30) is the plane wave expansion method [58].

The dispersion relation in a periodic structure differs significantly from that of a homogeneous medium. In a homogeneous material, frequency and wavevector have a linear relationship across all frequencies. However, in periodic structures, certain frequency ranges, called bandgaps, are forbidden at wavevector values like π/a , $2\pi/a$, ..., $n\pi/a$, where n is an integer. At these points, known as Brillouin zone boundaries, light is reflected due to the Bragg condition, creating strong reflection bands.

In these structures, the waves (known as Bloch waves) generally propagate through the medium, except within the bandgap where they decay exponentially. Near the Brillouin zone boundaries, Bloch waves turn into standing waves. Simulations show that at the low-frequency edge of a band, energy tends to concentrate in the high refractive index regions, while at the

high-frequency edge, energy localizes in the low-index regions. For frequencies inside the bandgap, light cannot propagate and instead decays over a characteristic distance called the Bragg length. This length depends on the strength of the periodicity, specifically, the number of layers and the refractive index contrast in a fabricated photonic crystal. Strong photonic crystals, which have a high index contrast, exhibit shorter Bragg lengths for bandgap frequencies.

These unique features of periodic structures give rise to valuable physical phenomena and applications. For example, the density of optical states drops to zero within the bandgap and increases near the band edges. This can enhance non-linear optical effects, making engineered photonic crystals especially useful for advanced optical devices.

3. Methodology

3.1. Modelling

3.1.1. Multilayer stacks and Photonic Band Gap model

To design a proper 1D PhC which works in the desired wavelength range suitable for the applied UCNPs, we need to find the refractive indices and thicknesses of each stack for the ML, transmitting excitation wavelength at 976nm and reflecting emission wavelength at 540nm. This model can be designed through two applicable methods which are discussed below in detail.

Transfer Matrix Method (TMM)

The TMM is a widely used analytical tool in optics and photonics for modeling the propagation of electromagnetic waves through layered structures, such as dielectric stacks and photonic crystals. It works by relating the electromagnetic field components, typically the electric and magnetic fields at the start of a multilayer system to those at the end. This is done by sequentially applying interface and propagation matrices for each layer and boundary. The method is based on Maxwell's equations, which impose continuity conditions on the electric and magnetic fields at material interfaces.

To analyze the reflection and transmission of a light wave through a multilayers' structure using the TMM, we can consider a 1D PhC made of alternating dielectric materials with different refractive indices and thicknesses. As illustrated in Fig. 8, multilayers consisting high-index layer (n_H) with thickness t_H and low-index layer (n_L) with thickness t_L, is positioned between air (n₀) and a substrate (n_s). The structure has a periodicity defined by $\Lambda = t_L + t_H$.

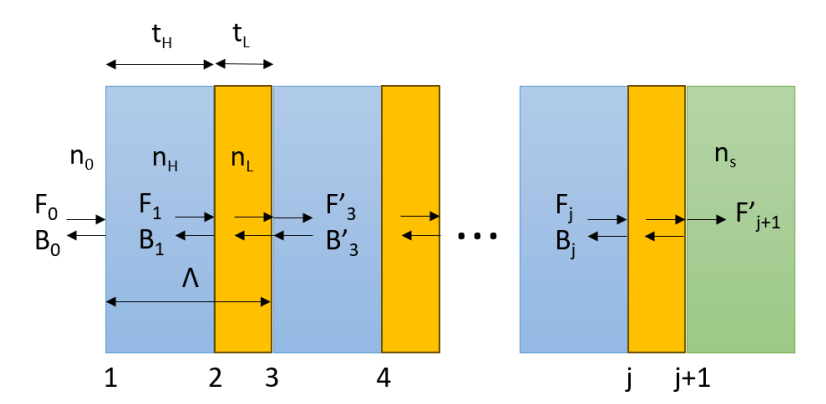


Fig. 8. The schematic diagram of a multilayer system.

When a light wave is incident on multilayers' structure, multiple reflections and transmissions occur at each interface. According to Fig. 8, in each layer j, we describe the wave using two components: a forward-propagating wave (to the right) with amplitude F_j , and a backward-propagating wave (to the left) with amplitude B_j .

At each interface j between two adjacent layers, the electric field must satisfy boundary conditions derived from Maxwell's equations. These conditions are captured by the interface matrix, which connects the wave amplitudes on either side of the interface [61]:

$$\binom{F_j}{B_j} = M_j^{-1} M_{j+1} \binom{F'_{j*1}}{0}$$
 (3.1)

Here, M_j is the matching matrix (also known as the dynamical matrix), which differs depending on the wave polarization:

$$M_{j} = \begin{cases} \begin{pmatrix} 1 & 1 \\ n_{j} \cos \theta_{j} & -n_{j} \cos \theta_{j} \end{pmatrix} & \text{, for TE waves} \\ \begin{pmatrix} \cos \theta_{j} & \cos \theta_{j} \\ n_{i} & -n_{i} \end{pmatrix} & \text{, for TM waves} \end{cases}$$
(3.2)

Inside each layer j (of thickness t_j), the wave undergoes a phase shift while propagating. This is described by the propagation matrix P_i :

$$\binom{F'_{j+1}}{B'_{j+1}} = P_{j+1} \binom{F_{j*1}}{B_{j+1}}$$
 (3.3)

Where;

$$P_{j+1} = \begin{pmatrix} e^{ik_{x,j+1}t_{j+1}} & 0\\ 0 & e^{-ik_{x,j+1}t_{j+1}} \end{pmatrix}$$
(3.4)

By combining the interface and propagation matrices recursively, we can construct the global transfer matrix for the entire multilayer system:

$$\binom{F_0}{B_0} = \left[\prod_{1}^{N} P_{j+1} M_j^{-1} M_{j+1}\right] \binom{F_{N*1}}{0}$$
 (3.5)

Where F_0 , B_0 are the amplitudes of the incident and reflected waves at the front surface, F_{N*1} is the transmitted wave amplitude at the last layer, N is the total number of internal layers.

From this system matrix, we can extract the reflection and transmission coefficients by applying appropriate boundary conditions at the input and output media.

The overall transfer matrix M of a multilayer system is obtained by the product of the interface (dynamical) and propagation matrices for all layers in the system. This matrix connects the total wave amplitudes at the front and back of the multilayer stack.

The relation between the incoming and outgoing wave amplitudes can be expressed as:

$$\begin{pmatrix} F_0 \\ B_0 \end{pmatrix} = M \begin{pmatrix} F_{N*1} \\ 0 \end{pmatrix} = \begin{pmatrix} M_{11} & M_{12} \\ M_{21} & M_{22} \end{pmatrix} \begin{pmatrix} F_{N*1} \\ 0 \end{pmatrix}$$
 (3.6)

Here, F_0 and B_0 are the amplitudes of the forward (incident) and backward (reflected) waves at the front of the structure, and F_{N*1} is the amplitude of the transmitted wave at the output interface. Since there is no incoming wave from the output medium, the backward amplitude B_N+1 is zero.

From this, we derive the reflection and transmission coefficients:

$$r = \frac{B_0}{F_0} = \frac{M_{21}}{M_{11}} \tag{3.7}$$

$$t = \frac{F_{N+1}}{F_0} = \frac{1}{M_{11}} \tag{3.8}$$

Where, r and t are the reflection and transmission coefficients respectively.

Consequently, these expressions allow us to compute the reflectance ($R = |r|^2$) and transmittance ($T = |t|^2$) of the structure, based on the system matrix elements and the boundary conditions.

Finite Element Method

The Finite Element Method is a powerful numerical technique widely used to solve partial differential equations arising in physics and engineering, particularly in complex geometries or with inhomogeneous materials. In electromagnetics, FEM is employed to solve Maxwell's equations either in the time or frequency domain, making it well-suited especially for photonic crystal analysis where material interfaces and boundary conditions play critical roles.

FEM works by discretizing the simulation domain into a finite number of small subdomains, called elements in meshing (typically triangles in 2D) and solves the governing equations over each element using variational methods. Within each element, the field quantities (e.g., the electric field) are approximated using interpolation functions, and the integral form of Maxwell's equations is solved over the entire domain. This approach provides high accuracy in handling curved interfaces and varying refractive indices, conditions that are typical in photonic crystals.

The general wave equation for the electric field in frequency domain, assuming harmonic time dependence $e^{-i\omega t}$, is [62]:

$$\nabla \times \left[\frac{1}{\mu_r} \nabla \times E \right] - k_0^2 \varepsilon_r E = 0 \tag{3.9}$$

where μ_r and ε_r are the relative permeability and permittivity of the medium, and $k_0=\frac{\omega}{c}$ is the free-space wave number.

FEM reformulates this into a matrix eigenvalue problem, which can be solved numerically to obtain the eigenfrequencies and field distributions of photonic modes within the crystal.

In this model, we use the periodic structures in wave optic module of COMSOL through setting the periodic boundary conditions on the lateral walls in a unit cell. For this design (Fig. 9), a time-harmonic plane wave was launched into the simulation domain using an excitation port positioned at the bottom of the computational window, where the fused silica as the substrate located.

To compute the transmittance, a second port was placed at the top of the simulation domain. Both ports were set as periodic ports, allowing the definition of the wave vector in line with the periodicity of the structure. The model employed Floquet periodicity, which accounts for the phase shift between tangential field components that arises when the wave is incident at an angle. This phase shift depends on the wave vector and the spatial separation between the ports, making Floquet periodicity ideal for simulating plane wave interactions with periodic structures.

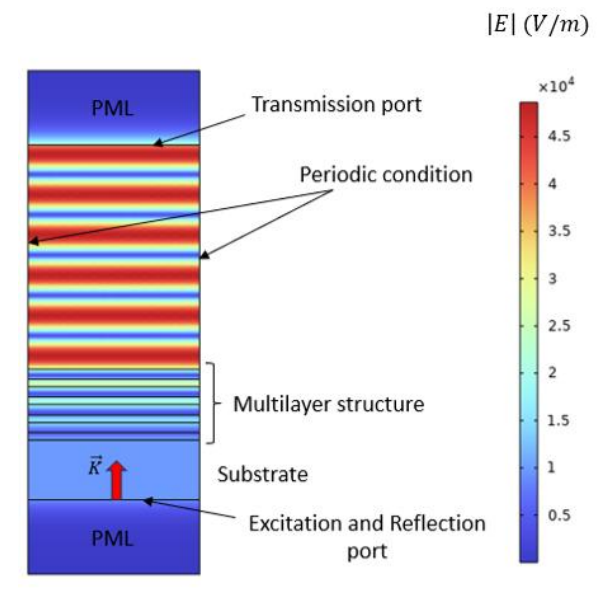


Fig. 9. Model of a unit cell of the designed multilayer system in COMSOL Multiphysics excited with a TM-polarized plane wave from bottom (substrate). Perfectly matched layers (PMLs) are used to absorb outgoing waves and prevent artificial reflections.

The simulation solved Maxwell's equations in the frequency domain, assuming that all materials involved were linear, isotropic, and nonmagnetic. For the material selection, the refractive indices of bi-layers including TiO_2 and SiO_2 were used according to the values defined in the MATLAB code from TMM. The dispersion curves $n(\lambda)$ used for dielectrics are shown in Fig. 10.

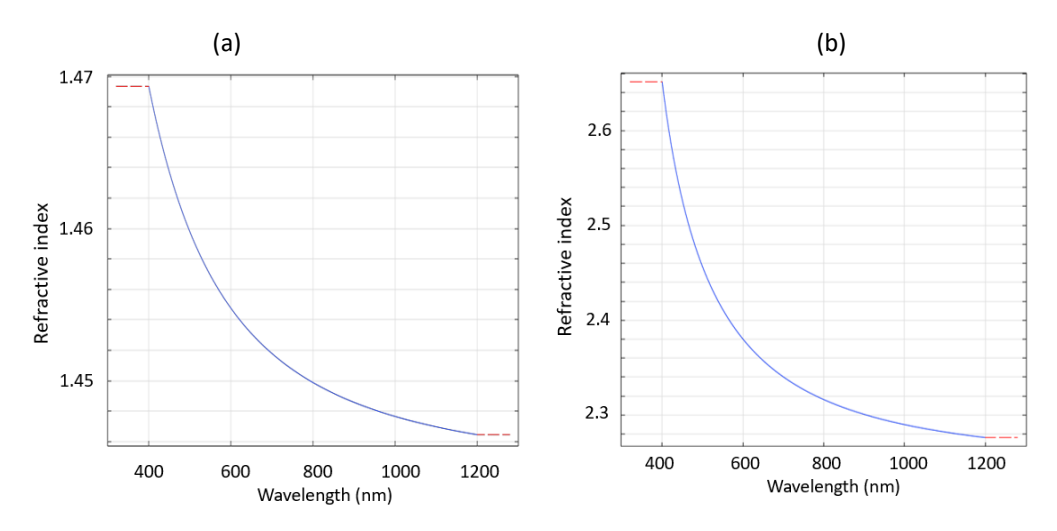


Fig. 10. Dispersion relation of (a) SiO2 and (b) TiO2 with alternating refractive index to the wavelength ranging from 400nm to 1200nm.

3.1.2. Gold Grating model

Having the multilayer structure with the desired PBG to act as an optical mirror, we can continue the FEM model with the grating structure to calculate the local electric field confinement for enhancement of surface plasmon resonances in the excitation process.

The dielectric response of metals can be modeled using the Drude and Lorentz–Drude models, which describe free electron behavior and interband transitions, respectively. However, these models use Lorentzian oscillators and may require many terms to accurately capture the optical behavior of noble metals like gold. To overcome this, the Brendel–Bormann (BB) model extends the Lorentz–Drude formulation by replacing sharp Lorentzian lines with a Gaussian distribution of oscillators, providing a better fit to experimental data [63].

The Drude model dielectric function of metals is:

$$\varepsilon(\omega) = 1 - \frac{\omega_p^2}{\omega^2 - i\Gamma\omega}$$
 (3.10)

The Lorentz–Drude model adds interband transitions:

$$\varepsilon(\omega) = 1 - \frac{\Omega_p^2}{\omega^2 + i\Gamma_0 \omega} + \sum_{j=1}^k \frac{f_j \omega_p^2}{\left(\omega_j^2 - \omega^2\right) + i\omega\Gamma_j}$$
(3.11)

where k is the number of oscillators with frequency ω_j , strength f_j , and damping frequency Γ_i .

The Brendel–Bormann model replaces the Lorentzian terms with Gaussian-broadened contributions:

$$X_{j}(\omega) = \frac{1}{\sqrt{2\pi}\sigma_{j}} \int_{-\infty}^{+\infty} \frac{f_{j}\omega_{p}^{2} exp\left[-\frac{(\omega'-\omega_{j})^{2}}{2\sigma_{j}^{2}}\right]}{(\omega'^{2}-\omega^{2})+i\omega\Gamma_{j}} d\omega'$$
 (3.12)

$$\varepsilon(\omega) = 1 - \frac{\Omega_p^2}{\omega^2 + i\Gamma_0 \omega} + \sum_{j=1}^k X_j(\omega)$$
 (3.13)

In COMSOL Multiphysics, the Brendel–Bormann model is implemented as a predefined option for gold. Since it shows excellent agreement with parameters and calculations obtained from Rakic *et al.* [63], according to the equations (3. 11) and (3. 12) especially in the visible range, making it the most accurate choice.

Following the wave Eq. (3. 9), the dielectric properties of the media; air and gold, were obtained from COMSOL Multiphysics' built-in material library. Air was modeled with a constant dielectric value of 1, while gold was represented using the Brendel–Bormann model. Similar to the FEM model of multilayer in a periodic structure, we create a gold grating over it in a unit cell with applying periodic boundary conditions and Floquet periodicity (Fig. 11 (a)). In this study, the mesh for the simulation was generated using COMSOL's physics-controlled meshing feature, shown in Fig. 11 (b). To ensure high accuracy in capturing the electromagnetic field distribution, especially near interfaces and fine structural features, the element size was set to 'Extra Fine'. This setting allows the meshing algorithm to automatically adapt the mesh density based on the physical properties and geometry of the model, providing a balance between precision and computational efficiency.

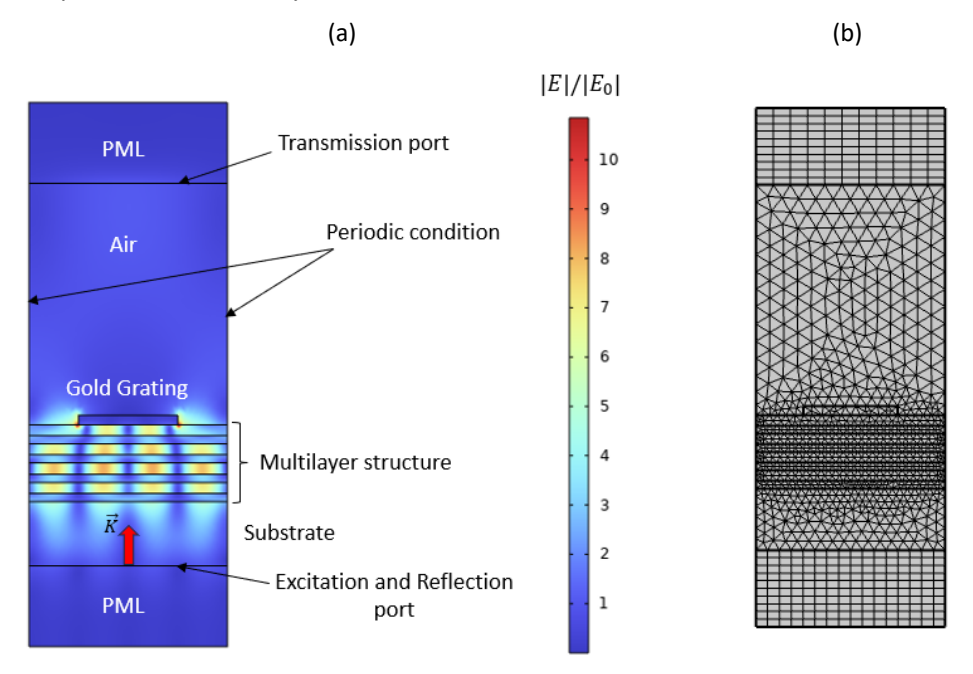


Fig. 11. (a) Model of the unit cell of multilayer along with the gold grating structure in air using periodic condition. (b) Model meshing.

In Fig. 11 (a), the color bar represents the electromagnetic field distribution using a comparable dimensionless value, $|E|/|E_0|$, which denotes the field enhancement factor (EF). This normalization reflects how structural variations in the gold nanostructure parameters including grating thickness, periodicity and duty cycle influence local field amplification, independent of absolute field strength or excitation wavelength.

3.1.3. Decay rate model

The decay rate model illustrated in Fig. 12 was employed to evaluate the decay rates associated with the green emission of $\rm Er^{3+}$ ions and the overall decay rate of Yb³⁺ ions. In the simulation, each dopant ion was modeled as a single, isolated, infinitely small electric dipole oscillating in a randomly oriented direction. To reflect the assumption that UCNPs are non-interacting and spatially isolated, only

one dipole source was placed within the computational domain. The decay rates were averaged over multiple dipole directions and positions to capture the lowest decay rate meaning the highest emission rate by the multilayers' effect on directionality. Periodic boundary conditions were not applied, as they would artificially replicate the dipole across the domain, leading to nonphysical periodic interactions. Instead, PMLs were implemented on all boundaries (top, bottom, right, and left) to absorb outgoing waves and simulate an open, infinite environment. The size of the simulation domain was chosen to be sufficiently large to enable accurate far-field analysis. The meshing settings for this model matched those used in the previous periodic structure simulation.

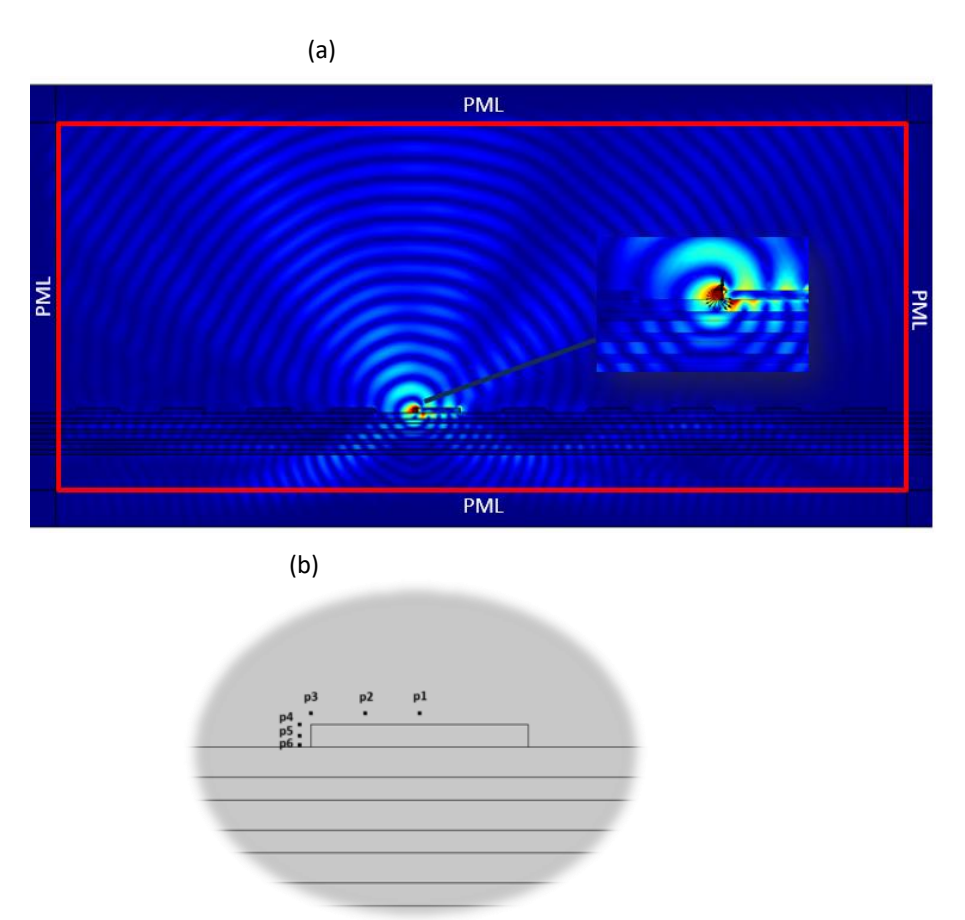


Fig. 12. Model for calculating decay rates; (a) the black arrows indicate the Poynting vectors and the red rectangle indicate the far field calculation, (b) in different dipole positions.

To estimate the quantum yield of UCNPs positioned near plasmonic structures, the model shown in Fig. 12 was simulated at the emission wavelength of 540 nm, and UCNPs emit photons isotropically. However, due to the limited numerical aperture of the objective with collection angle of 16.5° [17], we modeled the dipole emission within this angular range from -16.5° to $+16.5^{\circ}$.

The radiative power emitted into the far-field by the electric dipole in free space or near plasmonic structure was determined by integrating the Poynting vector S over the far-field boundary (highlighted by the red rectangle in Fig. 13

(a)):

$$P_r = \int_A S. \, dA \tag{3.14}$$

The presence of the gold grating introduces non-radiative losses due to absorption, which were computed by integrating the ohmic loss density Q_e over the volume of the grating:

$$P_{abs} = \int_{V} Q_{e}. \, dV \tag{3.15}$$

According to Poynting's theorem, the radiative and absorptive decay rates of a dipole emitter are proportional to the emitted or absorbed power normalized by the square of the dipole moment [63]. Specifically:

$$\Upsilon_{\rm r}^0 \propto \frac{P_r^0}{2|\rho_{em}|^2}, \Upsilon_{\rm r}^p \propto \frac{P_r^p}{2|\rho_{em}|^2}, \Upsilon_{\rm abs}^p \propto \frac{P_{abs}^p}{2|\rho_{em}|^2}$$
(3.16)

Where ρ_{em} is the dipole moment of the emitter. Followingly, P_r^0 and P_r^p are radiated powers from the dipole in free space and near a plasmonic structure, respectively (calculated by the equation (3. 14)). Also, P_{abs}^p that is the power absorbed by the plasmonic structure from the dipole (calculated by the equation (3. 15)).

In essence, this relationship expresses how the radiative and absorptive decay rates of an emitter are affected by its environment (particularly by nearby plasmonic materials) based on the time-averaged power flow associated with the dipole.

Finally, by inserting the Eq. (3. 16) into Eq. (2. 28) the quantum yield enhancement q_p in the presence of the plasmonic structure was calculated using the following expression in terms of power:

$$q_p = \frac{(P_r/P_r^0)}{\left[\left(\frac{P_r}{P_r^0} \right) + \left(\frac{P_{abs}}{P_r^0} \right) + \frac{(1 - q_0)}{q_0} \right]}$$
(3.17)

The ratio q_p/q_0 is commonly used to quantify the quenching or enhancement of quantum yield (QY) in the presence of environmental effects, such as proximity to plasmonic structures or quenching surfaces. Here, q_0 represents the intrinsic QY of the emitter in free space which is known and equals to 0.03 according to the studied value from the last work [17], while q_p is the QY under the modified conditions. This ratio reflects how the radiative and non-radiative decay processes are altered. Since quantum yield is defined as $q_0 = \Upsilon_r^0/(\Upsilon_r^0 + \Upsilon_{nr}^0)$, any change in either the radiative or non-radiative (absorptive) decay rates due to environmental coupling will impact q_p through relationship expressed in equation (3. 16). A ratio $q_p/q_0 < 1$ indicates quenching (reduced emission efficiency), while $q_p/q_0 > 1$ suggests enhancement through radiative rate increase or suppression of non-radiative losses. This metric provides a concise and intuitive way to evaluate the effect of the surrounding environment (plasmonic materials and multilayers) on the emitter's performance [64].

3.2. Fabrication

In this work, we report the fabrication of an optical multilayer structure composed of four alternating bilayers of silicon dioxide (SiO_2) and titanium dioxide (TiO_2), capped with a patterned gold grating (Fig. 13). The ML stacks are designed to exhibit tailored optical properties suitable for photonic or plasmonic applications. To achieve high precision and conformality in thin-film deposition, the dielectric multilayers were grown using plasma-enhanced atomic layer deposition (ALD), ensuring accurate control over thickness and composition at the nanometer scale. The metallic grating structure was subsequently defined on top of the multilayers using high-resolution electron beam lithography (EBL), followed by a metal deposition and lift-off process to emerge well-defined nanoscale patterns.

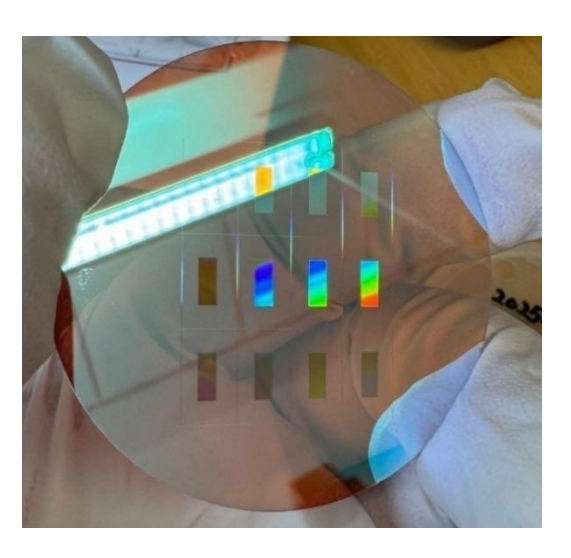


Fig. 13. ML-deposited on a fused silica wafer and patterned with the 3x4 matrix of grating structures.

To ensure the reliability and accuracy of ALD fabrication step, we employed spectroscopic ellipsometry for the test samples to calibrate the indicating parameters in ALD machine to achieve the desired thickness of the multilayers. As well as scanning electron microscopy (SEM) to verify the structural integrity and pattern fidelity of the gold gratings. This combination of advanced deposition, lithography, and metrology techniques enables the precise realization of complex nanostructures, laying the foundation for exploring their optical and plasmonic behaviors.

3.2.1. Multilayer Structure Using Plasma-Enhanced ALD

The 1D PhC structure was fabricated using Plasma-Enhanced ALD on a 2-inch fused silica wafer, shown in Fig. 14 (a). The deposition process was performed using a TFS-200 system (Beneq, Finland), operated at a substrate temperature of 150 °C with a remote nitrogen plasma power of 100 W. The multilayer design comprised 4 bilayers of alternating TiO_2 and SiO_2 , beginning with TiO_2 as the first (bottom) layer and ending with SiO_2 as the topmost layer, resulting in a total film thickness of approximately 500 nm. The process involved cleaning, calibration, and deposition steps to ensure high optical performance and layer uniformity.

ALD Cycle Calibration Using Ellipsometry

Prior to fabricating the complete multilayers' structure, the deposition characteristics of the ALD process were calibrated to determine the precise deposition rate values for both TiO₂ and SiO₂.

For the calibration process, separate test Si chips were coated with 300 ALD cycles of TiO₂ and SiO₂, each, using the same conditions planned for the final stack.

Woollam VASE is a Variable Angle Spectroscopic Ellipsometer, shown in Fig. 14 (b), is a tool for characterization of film thicknesses, material optical constants such as $n(\lambda)$ and $k(\lambda)$ as well as the surface roughness.

In ellipsometry linearly polarized light is directed at the sample at an oblique incidence angle; after reflecting off the thin film surface, the light becomes elliptically polarized which is described by two parameters:

- \bullet Ψ (Psi): Related to the amplitude ratio of the p- and s-polarized light components
- Δ (Delta): Related to the phase difference between these components These parameters are measured across a range of wavelengths and are then compared to theoretical optical models. By fitting the data to a model consisting of known materials (e.g., silicon substrate with TiO_2 or SiO_2 layers), the film's thickness can be predicted with given refractive indices measured before.

Ellipsometry is extremely sensitive to sub-nanometer thickness changes and is ideal for process calibration, especially in techniques like ALD where film growth is atomic-scale.

By modeling the optical response of each film, the refractive index and thickness were extracted, yielding the average deposition rate growth-percycle (GPC) values:

Dielectric	Deposition rate (Å/cycle)
TiO ₂	0.5
SiO ₂	1.1

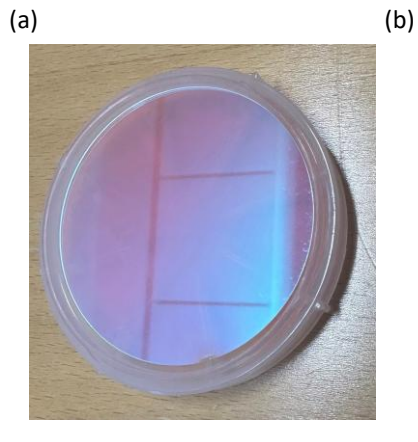




Fig. 14. (a) Fabricated 1D PhC on a 2-inch fused silica wafer. (b) Woollam VASE Spectroscopic Ellipsometer.

Substrate Cleaning and Surface Preparation

The fused silica wafers were first cleaned to remove organic and particulate contaminants and to promote good adhesion and uniformity during ALD growth. The cleaning procedure involved the following steps:

a. Organic Solvent Cleaning:

The wafers were sonicated for several minutes in acetone followed by isopropyl alcohol (IPA), each in an ultrasonic bath, to dislodge surface particles and dissolve organic residues.

b. Deionized (DI) Water Rinse:

After solvent cleaning, the wafers were rinsed thoroughly with DI water to remove solvent remnants, and was blow-dried by N₂.

c. Auto-Plasma Etching:

The wafers then underwent a 2-minute oxygen plasma etch in an automated plasma chamber. This step completely hydroxylated the surface and eliminated any possible contaminations that would affect the ALD process.

Backside Protection with Tape Masking

To prevent undesired deposition on the back side of the transparent fused silica wafer from the conformal ALD process, green adhesive tape was applied to cover the rear surface before loading it into the ALD chamber.

Before starting with the deposition process, the reaction chamber was first heated up the ALD to 150°C which left for one day to be stabilize the chamber environment. Then, the taped wafer was put in the chamber for about 1 hour to fix the tape on the wafer.

Multilayer Deposition via Plasma-Enhanced ALD

The ML stacks were deposited using a Plasma-Enhanced ALD system, which utilizes plasma-generated oxidizing species (typically oxygen radicals) to enable low-temperature, high-uniform film growth. Each ALD cycle consisted of four sequential steps:

- 1. Metal precursor pulse,
- 2. Nitrogen purge to extract any excess metal precursors,
- 3. Remote nitrogen plasma exposure along with oxygen gas feeding,
- 4. Nitrogen purge to extract by-product and excess oxygen gas.

This cycle was repeated for the desired number of times to achieve target thicknesses for each material. The machine with the settings in the Table 1 could start the deposition automatically.

	TiO₂ Deposition	SiO₂ Deposition
Precursor	Titanium	Bis(ethylmethylamino)silane
	tetrachloride (TiCl₄)	(BEMAS)
Oxidant	Plasma activated O ₂	Plasma activated O₂ gas
	gas	
Temperature	150°C	150°C
Plasma Power	100 W	100 W/

Table 1. Indicating parameters in the ALD technique-based deposition of the ML

As mentioned above, the fabricated ML stacks consisted of 4 bilayers of alternating TiO_2 and SiO_2 , beginning with TiO_2 as the first layer and terminating with SiO_2 on the top. The total optical structure had a physical thickness of approximately 500 nm, tailored to produce a 1D PhC with a stopband centered around the blue and green wavelengths. The required layer thicknesses were determined to be 51 nm for TiO_2 (high refractive-index material) and 68 nm for SiO_2 (low refractive-index material).

To translate these thicknesses into ALD cycle counts, previously determined deposition rate values were used: 0.5 Å/cycle for TiO_2 and 1.1 Å/cycle for SiO_2 , as measured via spectroscopic ellipsometry. The number of deposition cycles for each material was calculated using the formula; Number of cycles = desired thickness (in Å) / GPC. This resulted in:

- TiO₂: 510 Å / 0.5 Å/cycle = 1020 cycles
- SiO₂: 680 Å / 1.1 Å/cycle ≈ 618 cycles

These cycle numbers were used in the ALD recipe to fabricate each layer with high precision, ensuring the desired optical performance and periodicity of the multilayer structure.

3.2.2. Grating structure using electron-beam lithography

To enable optical functionality such as resonance coupling, spectral filtering, or out-of-plane scattering, the fabricated $\text{TiO}_2/\text{SiO}_2$ multilayer was patterned with a gold grating using EBL following with the lift-off process. EBL is a high-resolution patterning technique widely used in nanofabrication for creating features with dimensions down to a few nanometers. Unlike conventional optical lithography, which is limited by the diffraction of light, EBL employs a focused beam of electrons to directly write patterns onto an electron-sensitive resist. This makes it particularly suitable for fabricating intricate nanoscale structures, such as gratings, photonic crystals, and plasmonic components.

As depicted in Fig. 15, the process begins with spin-coating a positive electron-sensitive resist (e.g., Poly(methyl methacrylate) or PMMA) onto the sample, followed by deposition of a 30 nm conductive layer (copper) to prevent charging during exposure. In the next step, a focused electron beam is used to expose the desired pattern by locally modifying the solubility of the resist. After exposure, the conductive layer is removed by wet etching using diluted nitric acid (HNO₃). The sample then undergoes development, where the exposed resist regions are dissolved to reveal the underlying surface.

Subsequently, metal deposition is performed to coat the patterned area with gold. Finally, a lift-off process is carried out by immersing the sample in acetone to remove the remaining resist, leaving the metal features only in the exposed regions. Because EBL is a maskless, direct-write technique, it provides excellent flexibility for prototyping and research-scale fabrication, although it is relatively slow and not ideal for large-scale manufacturing. Followingly, the grating structures shown on Fig. 13, were precisely fabricated using a standard EBL process scheme on Fig. 15 as described below.

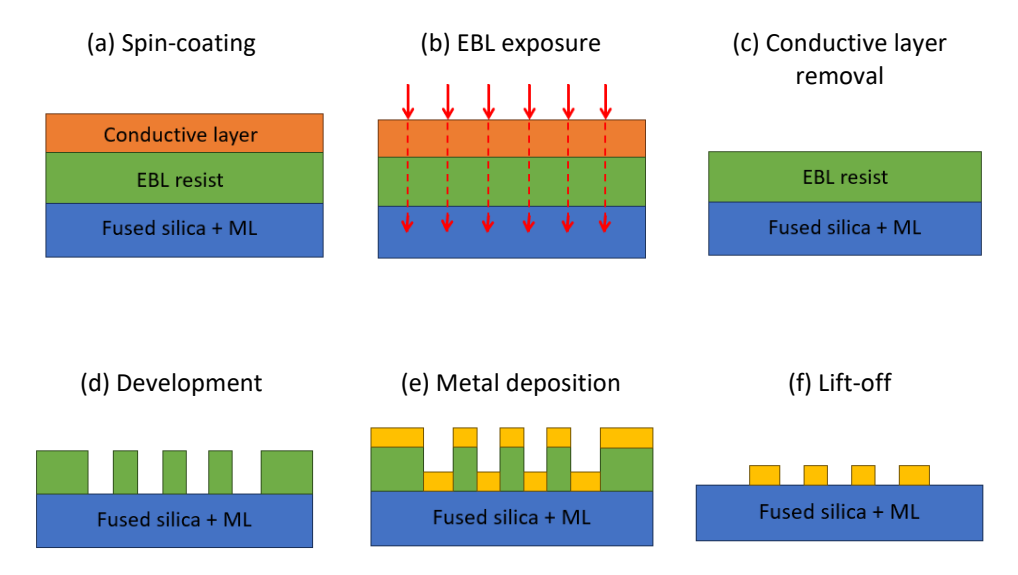


Fig. 15. Scheme of a typical electron beam (e-beam) lithography process.

a. Spin-coating of positive photoresist covered with a deposited conductive layer

The ML-coated fused silica wafer was first treated with a 2-minute O_2 plasma to enhance surface cleanliness and promote better resist adhesion. Following this, a layer of diluted positive photoresist (AR-P 672, Allresist GmbH, Germany) was spin-coated using a Laurell WS-650MZ-8NPPB spin coater (Lansdale, PA, USA) at 3000 rpm for 60 seconds. The coated wafer was then soft-baked on a 150 °C hot plate for 3 minutes to remove residual solvents and stabilize the resist film. A 30 nm-thick copper conductive layer was then deposited onto the resist layer using a Q300TT Plus coater (Quorum, UK).

b. E-Beam exposure for grating patterning

After soft baking, the wafer was fixed on a copper plate to avoid electron accumulation and mounted into the EBL system, then the grating structures depicted in Fig. 16 were patterned into the resist by EBL using a Vistec EBPG5000+HR system (Dortmund, Germany).

- Pattern area: 11 matrix grating structures with area of 2mm x 5mm, each in a 3x4 square matrix was written at the center of the wafer, with intentional side gaps to avoid edge defects and ensure clean lift-off.
- Grating design: According to the design from the FEM simulation in COMSOL,

- a 1230-nm grating with a groove depth of 60 nm and a duty cycle of 50 % was patterned.
- Exposure parameters: Operated at an acceleration voltage of 100 kV with an exposure dose of 900 μ C/cm².

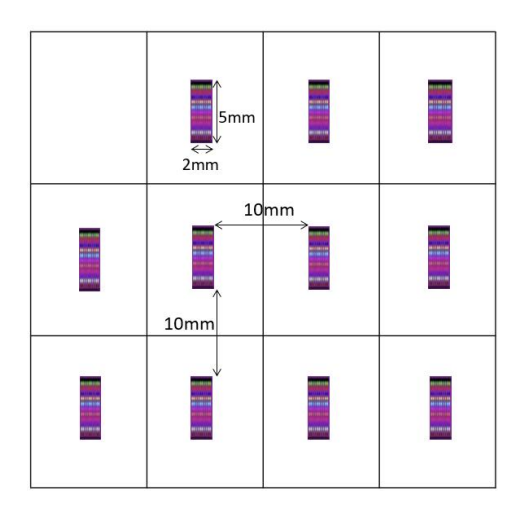


Fig. 16. Grating structure's pattern area.

c. Conductive layer removal

After exposure, the copper layer was first removed by soaking the wafer in a diluted HNO₃ solution for 30 s, followed by rinsing in DI water.

d. Development

The pattern was developed in a solution of isopropanol and methyl isobutyl ketone (IPA:MIBK, 3:1 by volume) for 60 s, followed by a 30 s soaking in pure isopropanol and a final rinse with DI water.

e. Metal Deposition

The patterned wafer was first coated with a 3 nm chromium adhesion layer, followed by the thermal deposition of a 60 nm gold layer using a MiniLab STO26A R&D Magnetron Sputtering and Thermal Evaporation System (Moorfield Nanotechnology, UK).

f. Lift-Off

After deposition, the wafer was soaked in acetone overnight to lift off the unwanted metal. The remaining photoresist was removed by gently agitating and sonicating the sample for 5 seconds. Finally, the wafer was rinsed with IPA and DI water and dried under a nitrogen gas flow, forming the final gold grating structure.

At the end of the ALD procedure, SEM was performed to evaluate the structural quality of both the fabricated gold gratings and the ML stacks. The SEM image of the ML shown in Fig. 17 (a) revealed some surface roughness in the top three layers, which is likely due to mechanical damage introduced during the cleaving process. In Fig. 17 (b), the SEM image of the Au grating, rough edges were observed along the grating lines. This irregularity is attributed to the formation of Au islands during the evaporation step, which were subsequently removed along with the PMMA during the liftoff process. To improve the uniformity of the Au grating, a reduction in the gold deposition

rate from 1.1 Å/s to 0.6 Å/s is proposed. This adjustment is expected to decrease the size of the Au islands, resulting in smoother grating edges and better overall structural fidelity.

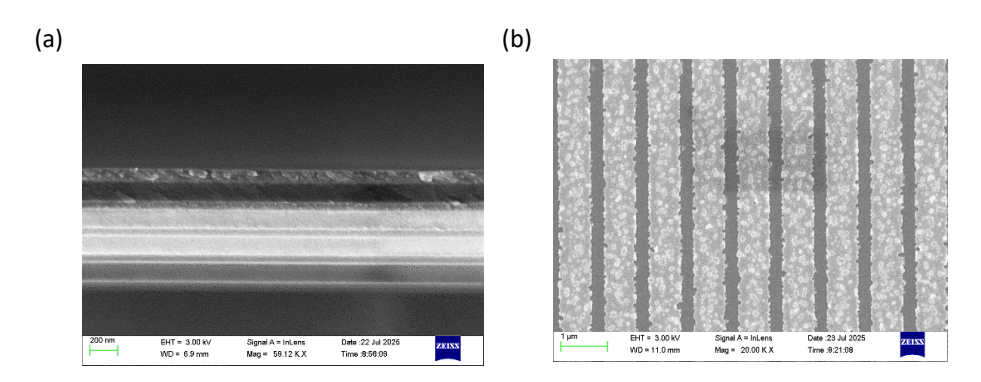


Fig. 17. SEM images from (a) stacks of multilayer, (b) grating structure.

3.3. Transmission Measurement

In order to ensure of the accuracy in functionality of band gap of the deposited multilayer, we measured the transmission spectrum of the fabricated ML stacks on the fused silica wafer by the spectrophotometer (PekinElmer Lambda 18) and compare it with the simulated spectrum in COMSOL. This way, we could proceed with the fabrication for grating structure on the ML stacks.

For the background correction, we first did the measurement with the instrument parameters stated in the Table 2 while the sample compartment was empty. Next, we repeated the measurement with the same parameters while having the wafer on the sample compartment.

Table 2. Parameters	of transmission measureme	nts

Wavelength range	400 nm – 850 nm
Mode	%T (transmission mode)
Average time	1.0 seconds
Data interval	0.5 nm
Baseline	Zero/baseline correction
Spectral bandwidth	2.0 nm
Auto polarizer	P for TM mode
	S for TE mode
Speed	120

4. Results and discussions

4.1. Multilayer's optical design and characterization

Using TMM approach in Matlab, a multilayer consisting 4 bi-layers of dielectrics SiO_2 and TiO_2 is modeled with thicknesses of 68 nm and 51 nm, respectively. As plotted in Fig. 18, the photonic band gap created by this model both in TE and TM modes can reflect and block the wavelengths in the PBG range including the desired Bragg reflector wavelength of 540 nm. This is the requirement for the emission of UCNPs to be reflected mostly by the mirroring effect of photonic crystal.

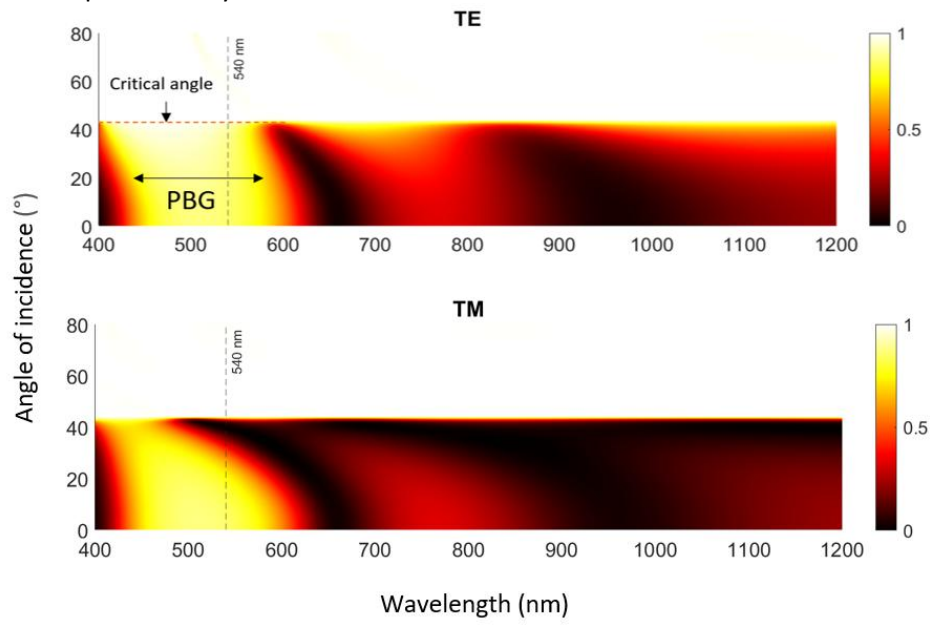


Fig. 18. The reflectance plots of the designed ML in TE and TM modes showing the wavelength range with high reflectance in PBG (yellow region) as a function of incident angle including the UC emission wavelength of 540 nm.

Following that, we had the FEM simulation results of the designed ML with desired PBG through plotting the transmittance spectrum and comparing it with the experimental results both in TM mode (Fig. 19) while transmitting light in normal incidence. The chart shows an acceptable compliance in the created band gap with our design, not only between two simulated and characterized spectra, but also with the reflectance plot from TMM approach (Fig. 18).

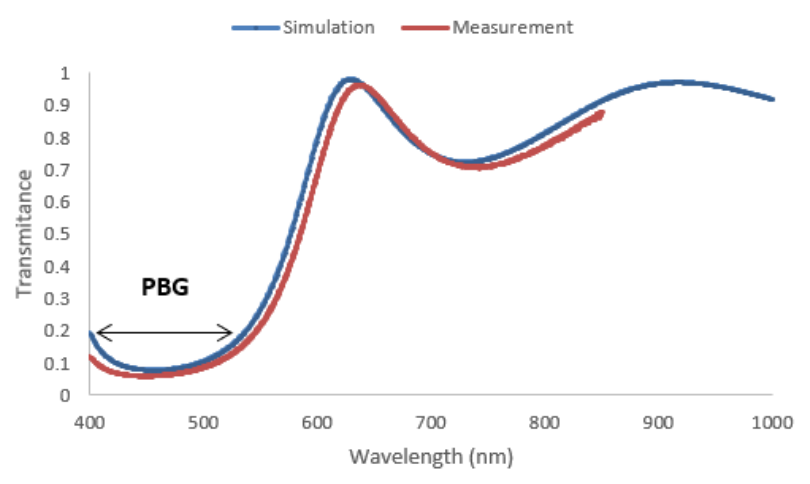


Fig. 19. Multilayer's transmittance spectra from simulation and measurement results.

4.2. Surface plasmon polariton excitation enhancement

4.2.1. Gold Grating characterization

To enhance the localized electric field in the grating structure with multilayer, it is essential to optimize the grating parameters illustrated in Fig. 20. Under TM polarization, the coupling of SPPs results in a pronounced dip in the reflectance spectrum around 976 nm. In contrast, no such dip appears under TE polarization, as SPPs cannot be excited in that mode. Therefore, all simulations aimed at identifying optimal SPP resonances are conducted under TM mode using the port mode setting. In the study by Le *et al.* [17], the grating coupling Eq. (2. 24) was employed to estimate the grating period required to excite SPPs at a 976 nm wavelength under normal incidence in air. The optimized structure featured a period (d) of 920 nm, a groove depth (g) of 55 nm, and a duty cycle (dc) of 80%.

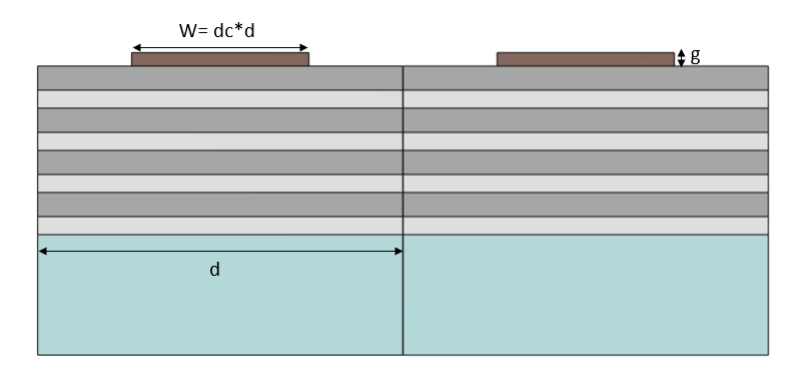


Fig. 20. Determining parameters in the gold grating structure; as g for groove depth, w for width and dc for duty cycle.

Therefore, we could also apply these preliminary parameters for the gold grating on the ML with FEM modeling to compare the results with and without ML. As shown in Fig. 21, working with multilayers and creating the desired PBG requires excitation of SPPs from bottom (substrate), while it was set to excite the SPPs from the top (air) without multilayers.

The electric field cross sections in Fig. 21 (a) shows SPPs have the similar field distributions on the gold grating with excitation wavelength of 976 nm.

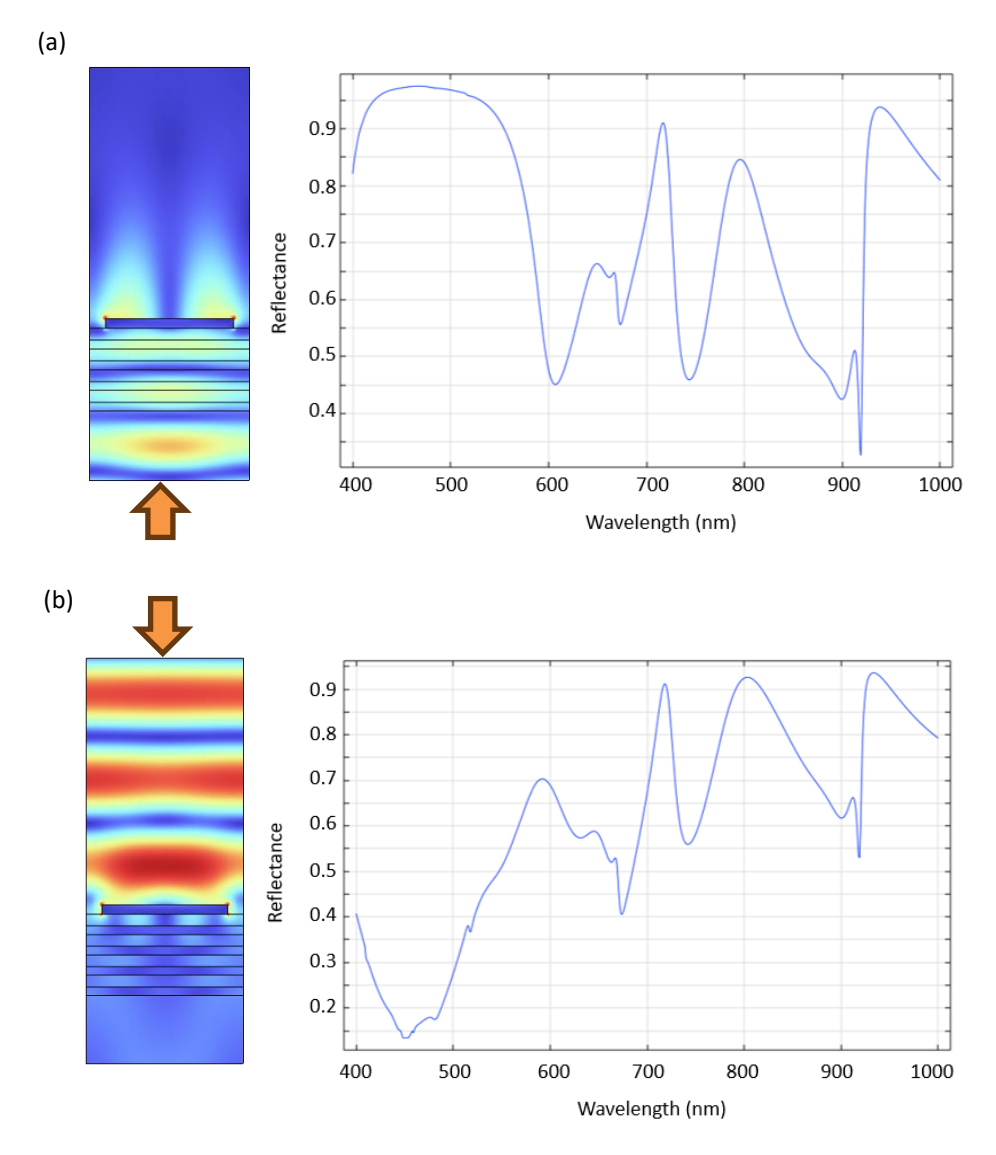


Fig. 21. Reflectance spectrum of SPPs over wavelength range of 400-1000 nm with (a) excitation from the substrate, (b) excitation from the air.

In the simulation, after comparing the results with the previous design [17], we tried to optimize the grating structure by altering determining parameters while applying our designed ML. We could analyze the effect of each parameter separately on the reflectance surface plot over the wavelength range and also the related enhancement factor to find the best resonances for SPPs. Therefore, we

studied three key parameters in grating structure that are as follow.

Grating thickness (g)

Alternation along the thickness of the grating shows no significant effect on the reflectance surface plot, illustrated in Fig. 22. This observation suggests that within the investigated range (30–60 nm), grating thickness is not a critical parameter for enhancing SPPs, particularly at the upper end of this range. Given that the EF remains largely independent of grating thickness, a fixed value of 60 nm was selected for subsequent simulations.

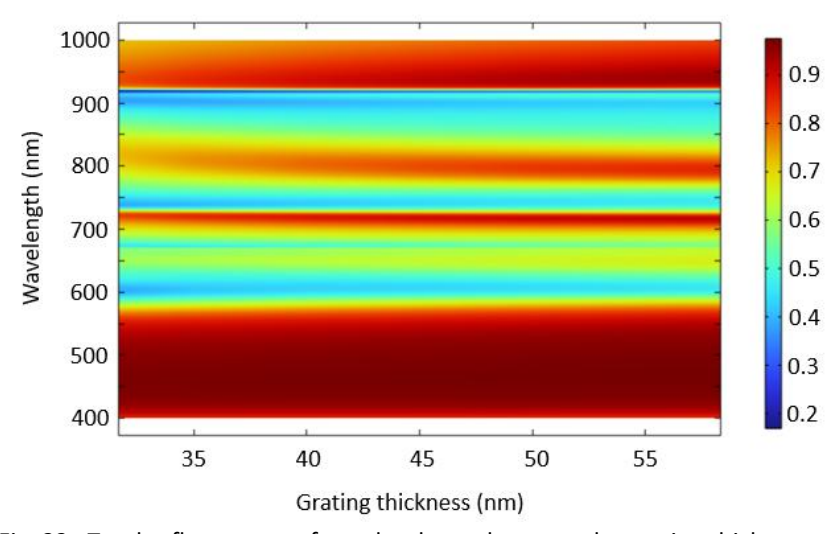


Fig. 22. Total reflectance surface plot dependence on the grating thickness over the wavelength range of 400-1000 nm.

Grating periodicity (d)

The next parameter investigated in Fig. 23 (a) and (b) is the grating periodicity for two different duty cycles, 0.8 and 0.5, respectively. The sweep was done on varied periodicities from 900 nm to 1400 nm in 50 nm increments, over a narrower wavelength range of 700–1000 nm. We can neglect the wavelengths less than 700 nm as PBG wavelength range (400-700 nm) is attributed to the UC emission and out of our consideration for the excitation enhancement, further it can help reduce software computation time. As illustrated in Fig. 23 (b), the distinct rising and falling region at the periodicity around 1200 nm in the surface plot can be directly related to the reflectance spectrum at this periodicity, which displays sharp peaks and dips corresponding to the Fano-like surface plasmon polariton resonances. These resonance features shift with changes in the grating periodicity, allowing for precise tuning to a desired excitation wavelength, specifically, 976 nm in this case.

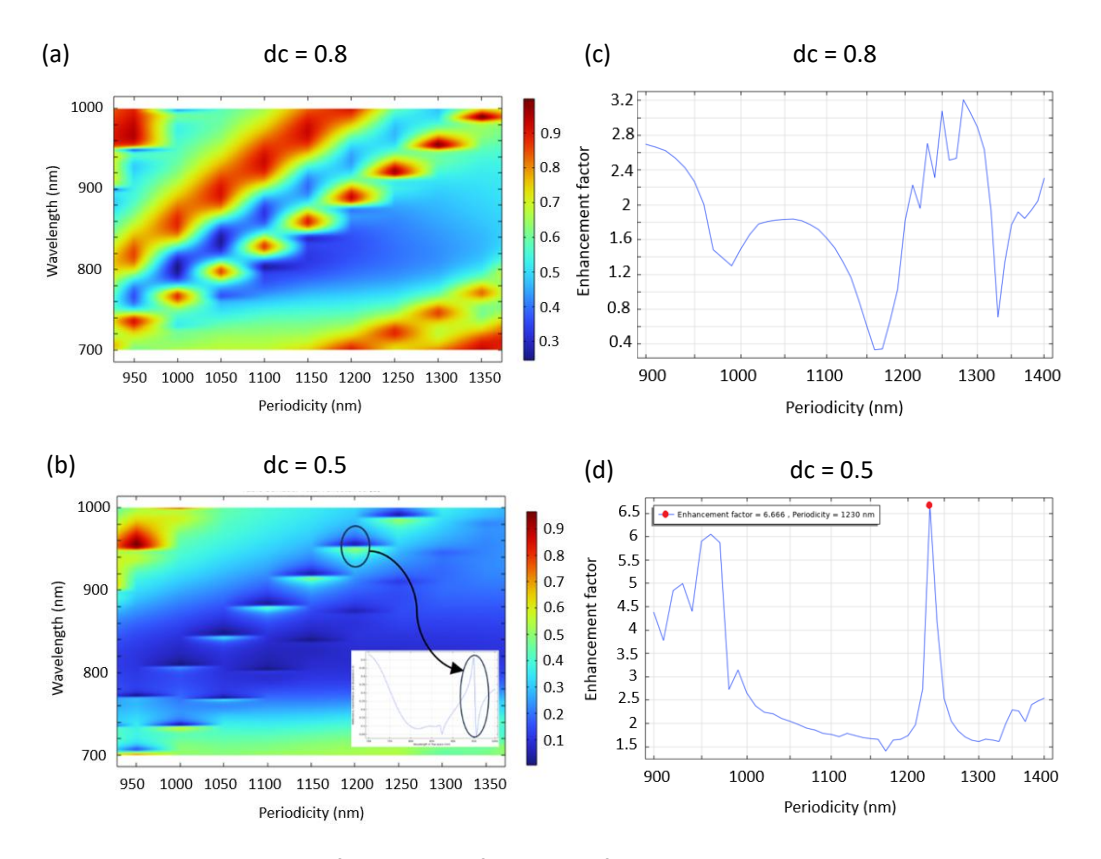


Fig. 23. Total reflectance surface plot of the grating periodicity alternation over wavelength range of 700-1000 nm with (a) duty cycle of 0.8, (b) duty cycle of 0.5 showcasing the peak and dip of the SSP resonances in the reflectance spectrum with d=1200. Enhancement factor graphs in accordance to the increasing periodicity for duty cycle of (c) 0.8, and (d) 0.5 with the highest value 6.666 at periodicity 1230 nm.

From the plots related to the duty cycle of 0.8, we can see no enhancement in the SPP resonances and they are fade out. While, gratings with duty cycle of 0.5 results in clear and sharp resonances. We can find the best resonance at excitation wavelength of 976 nm through extracting the highest EF in the plot (d), which shows the highest factor for 1230 nm periodicity with a value about 6.66.

After this step, we can continue the parameter studies for the duty cycle to find the final grating structure considering grating thickness and periodicity of 60 nm and 1230 nm, respectively.

Grating duty cycle (dc)

Duty cycle is another determining parameter which also accounts for the width of the grating and it is important to create enough interaction surface with the localized electric field. we studied the alternation of duty cycle from 0.1 to 0.9 for better comparison among the whole width ranges of the grating, which can be seen in the plots of Fig. 24. Although the plot (a) showcases lower reflectance rates for the duty cycles with values less than 0.5, the enhancement factor plot (b) gives the highest value at 0.5 which is also confirming the results from the former parameter study of periodicity.

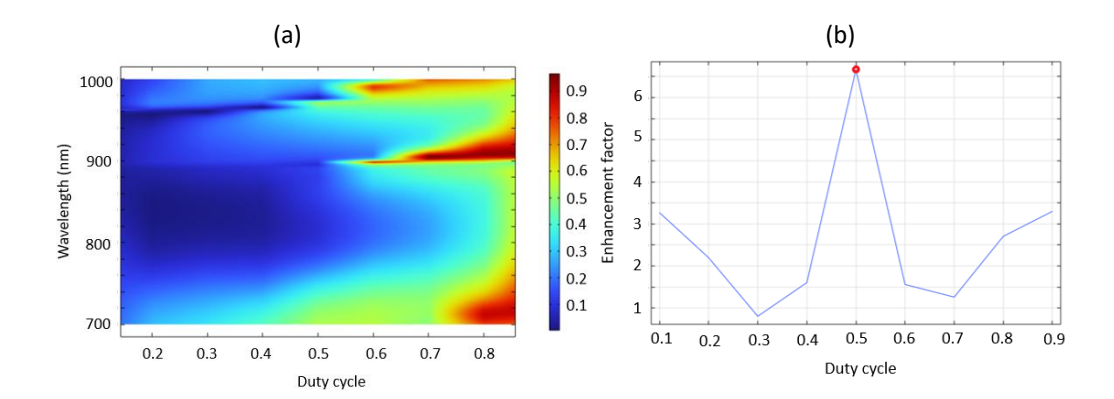


Fig. 24. (a) Total reflectance surface plot of the grating duty cycle alternation over the wavelength range of 700-1000 nm. (b) EF at excitation wavelength 976 nm with d=1230 nm.

Consequently, the final structure of the grating along with the designed multilayers in the simulation turns out the thickness (g) of 60 nm, the periodicity (d) of 1230 nm and the duty cycle (dc) of 0.5 for the highest enhancement in SPPs' resonances at the excitation wavelength of 976 nm. The electric field cross section of the final structure at TM mode is illustrated in Fig. 25, which clearly shows the SPPs around the groove edges of the grating. The color legend indicates the EF with the highest value of about 11 times.

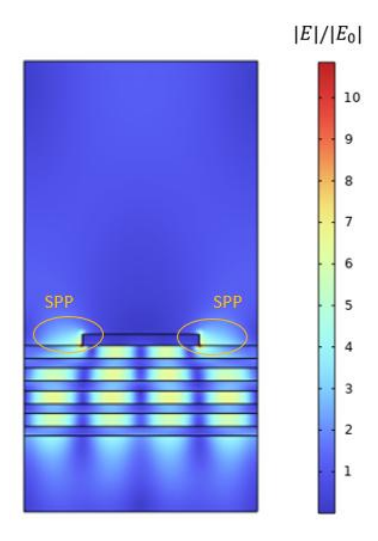
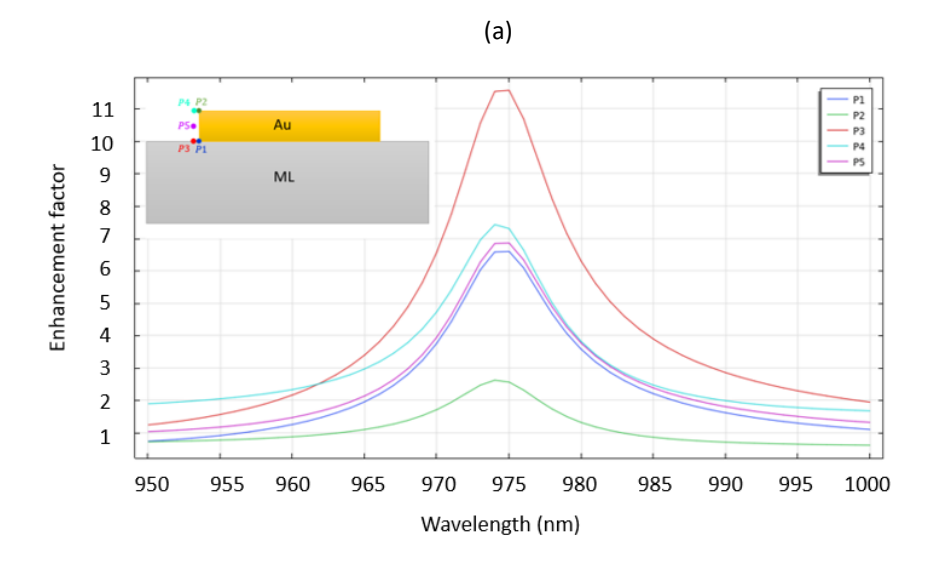


Fig. 25. The electric field cross section of the final nanostructure with the corresponding enhancement factor and SPPs at the excitation wavelength of 976 nm.

4.2.2. Electric field enhancement mapping

To gain a better understanding of the localised electric field enhancement along the side boundaries of the grating, particularly where the tails of the SPPs extend, we performed point evaluations at five distinct locations. These points (P1, P2, P3, P4, and P5) were primarily positioned within the grooves, where the SPP fields are

predominantly distributed along the sidewalls of the grating. As shown in Fig. 26 (a), the enhancement factors at these points reveal the spatial variation of field intensities around the grating structure. The trend of these enhancement peaks can be further analyzed through a linear cross-sectional profile of the grating thickness overlaid with the localised field distribution, as presented in Fig. 26 (b).



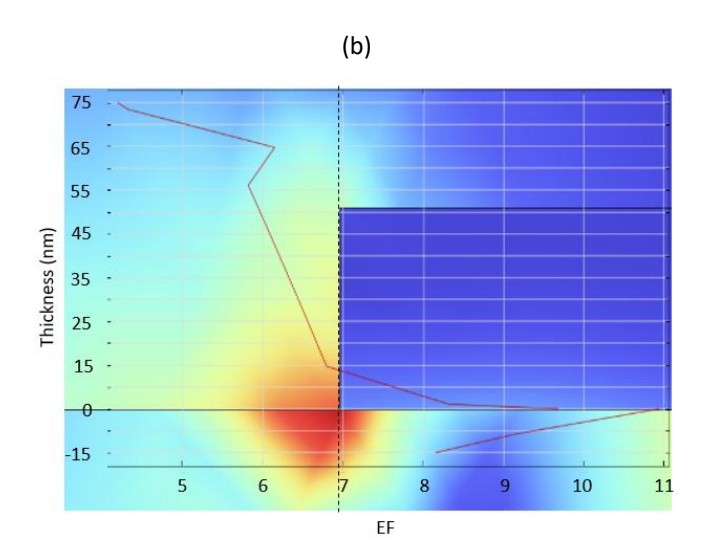


Fig. 26. The localised electric field enhancement (a) mapping of different points around the depicted grating, (b) along the determined cross section of the grating thickness.

4.3. Up-conversion emission enhancement

In line with the objective of this work, the application of multilayers is intended to enhance UC emission and directionality, primarily through the wavelength-selective properties or mirroring effect of photonic crystals. To investigate the impact of the added multilayer stack on the grating structure, UCNPs were initially modeled as electric dipoles. We then analyzed the resulting

enhancement by examining directionality and quantum yield at the UCNPs' emission wavelength of 540 nm.

4.3.1. Directionality

To evaluate directionality enhancement in multilayer structures, we simulated and compared four configurations with dipole emission, based on the far-field calculation in FEM modeling of decay rates described in Section 3.1. As shown in Fig. 27, the emission patterns of a dipole placed on various structures including; fused silica substrate, flat gold, a planar multilayer, and a grating-coupled multilayer structure are compared. The results demonstrate that the emitted light from multilayer-based structures is directed upward, regardless of the photonic crystal's permeability to TM modes transmitting a portion of light downward, even within the PBG region.

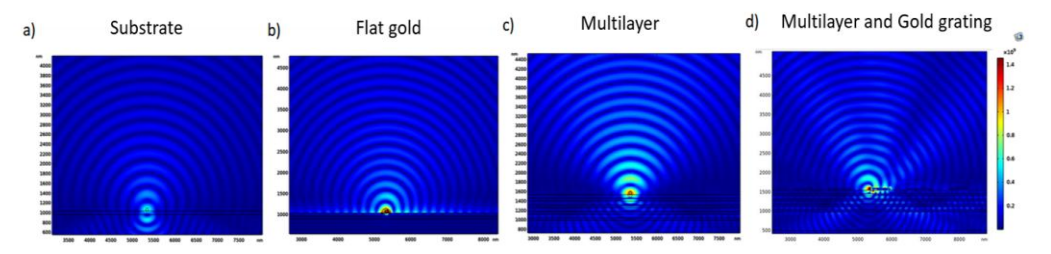
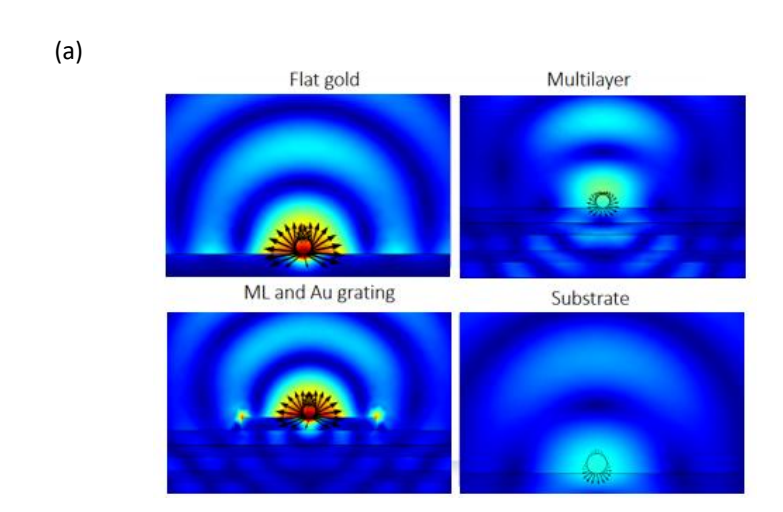


Fig. 27. The emission directionality for dipole on a a) substrate, b) flat gold, c) multilayer structure, and d) multilayer with grating structure.

In Fig. 28 (a), the Poynting vectors are shown in arrows for the four structures presented in Fig. 28, illustrating the radiative power of electric dipole emission as time-averaged power flow at the selected emission angle of 0°. Fig. 28 (b) compares the calculated power outflow through only the top surface over the full scattering angular range from -16.5° to 16.5° . This power is obtained via surface integration, as defined by Eq. (3. 14), and is then expressed as a ratio relative to the power outflow of the substrate structure, which serves as the reference baseline.



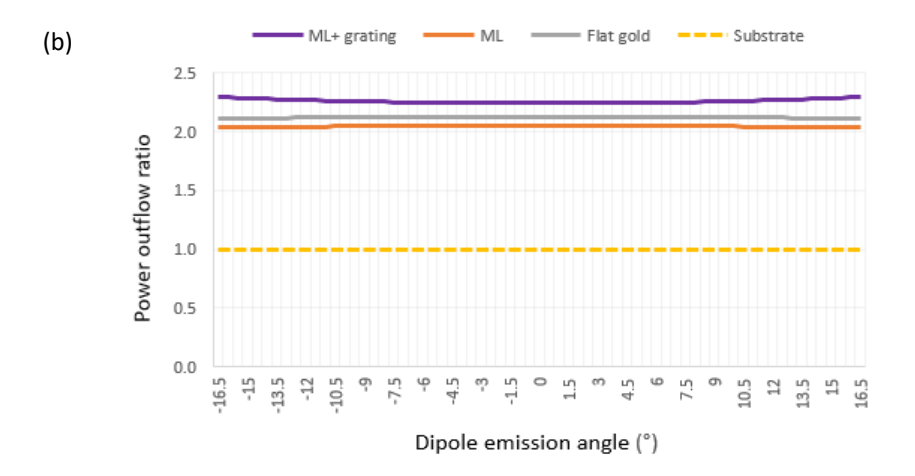
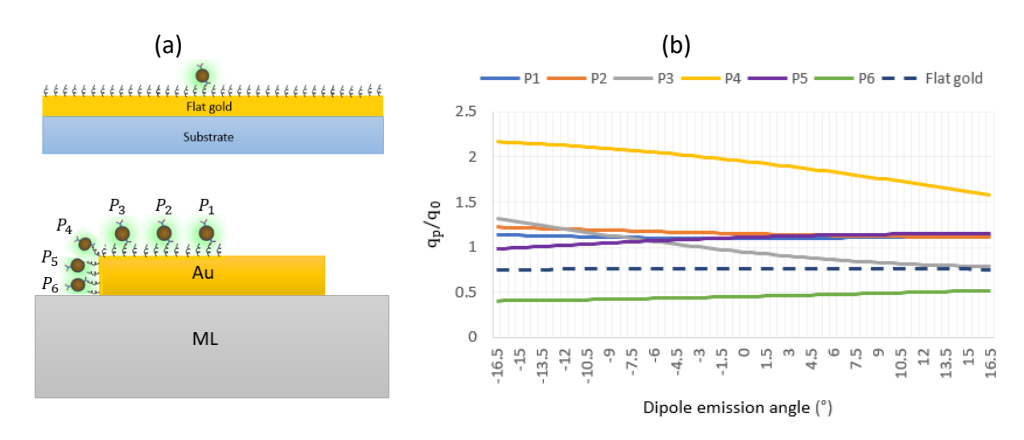


Fig. 28. (a) The Poynting vector for four different structures at the emission angle 0 $^{\circ}$, (b) the upward power output flow ratio normalized to the substrate's power for a full-scattering range of the emission angle from -16.5 $^{\circ}$ to 16.5 $^{\circ}$.

Despite the improved directionality achieved with the multilayer configurations, the calculated results show that these structures do not significantly enhance the power outflow compared to the flat gold case. This can be attributed to a portion of the power being lost to guided TM modes within the multilayer stacks.

4.3.2. Quantum yield

For the emission analysis, the next key step in evaluating the quenching effect of UCNPs involves calculating the quantum yield enhancement, expressed as the ratio q_p/q_0 , based on Eq. (3. 16) from the decay rate model. Fig. 29 represents the results of this analysis, comparing the designed grating structure to a flat gold reference. As shown in Fig. 29 (a), quantum yield calculations were performed at six different dipole locations to identify the optimal position for emission enhancement. The results in Fig. 29 (b) show that the highest enhancement occurs at position P4, where the QY ratio peaks around 2.2 at an emission angle of -16.5° , gradually decreasing to 1.6 at 16.5°. Other positions exhibit lower but more stable enhancements across angular range. In contrast, the flat gold surface yields QY ratios below 1, indicating significant quenching.



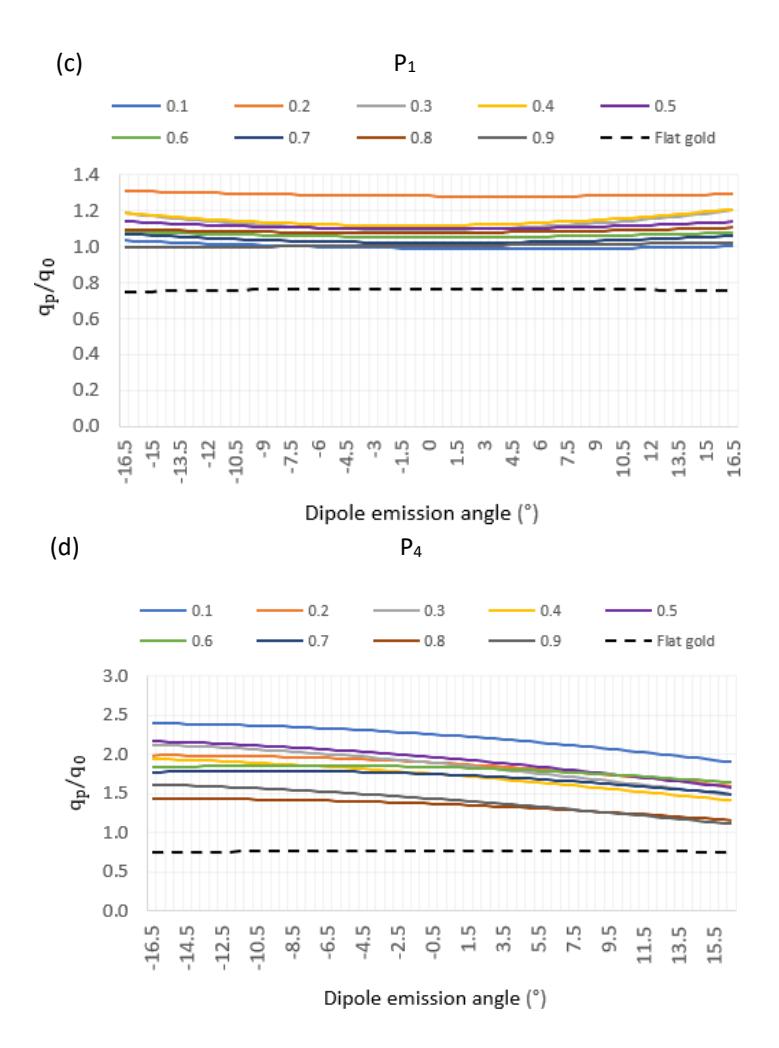


Fig. 29. Computational investigation of the quenching effect with a UCNP near a gold surface. (a) Illustration of the location of the UCNP on flat gold or on grating with six cases (P1, P2, P3, P4, P5, and P6). (b) The quenching effect of the UCNP on flat gold and on grating as a function of the dipole emission angle in six points. The quenching effect is evaluated by the quantum yield ratio of the UCNP near the gold surface (q_p) and in free space (q_0) . The dipole emission angle is determined by the collection angle of the used objective (±16.5°). The quenching effect with the duty cycle changes at the locations (c) P_4 and (d) P_1 .

To investigate the effect of duty cycle on quenching, we selected two dipole positions on the grating and recalculated the QY enhancement ratio. As shown in Fig. 29 (c), the QY enhancements at location P1 remain relatively consistent across all duty cycles with a narrow range from 1.0 to 1.3. In contrast, Fig. 29 (d) shows a slightly higher sensitivity to duty cycle variations at location P4, where the structure with a duty cycle of 0.5 exhibits the highest QY enhancement after the configuration with a duty cycle of 0.1.

We did not further explore the effect of changing the grating period on quenching, as such changes can shift the excitation wavelength away from the target value of 976 nm due to the influence of the multilayer stack.

5. Conclusions

In this work, we presented FEM modeling of excitation and emission enhancement, as well as the fabrication and characterization of grating and photonic crystal structures. The final simulated and fabricated nanostructure consists of multilayers with 51 nm of $\rm TiO_2$ and 68 nm of $\rm SiO_2$, patterned with the optimized gold gratings on top. Optimization of SPP excitation was achieved by varying grating parameters, revealing that Au thickness had minimal impact leading to a choice of 60 nm, while a periodicity of 1230 nm and duty cycle of 0.5 maximized the enhancement factor about to 11 times at the 976 nm excitation wavelength, which is not a significant improvement in excitation efficiency.

From the computational quenching effects, we found that there were a slight emission quenching effect and an increase in the 976-nm total decay rate when UCNPs were near the surface of the gratings and the flat gold, which makes insignificant contributions to UC enhancement. However, the dipole position at point P4 representing the UCNP's emission on the edge ridge of the grating, has the highest QY enhancement value of 2.17 with emission angle of -16.5° , as shown in Fig. 30. According to the comparison chart in Fig. 30 (a), this value shows about twofold increase to the emission enhancement of the last work's highest quenching effect ratio, which was about 1.1.

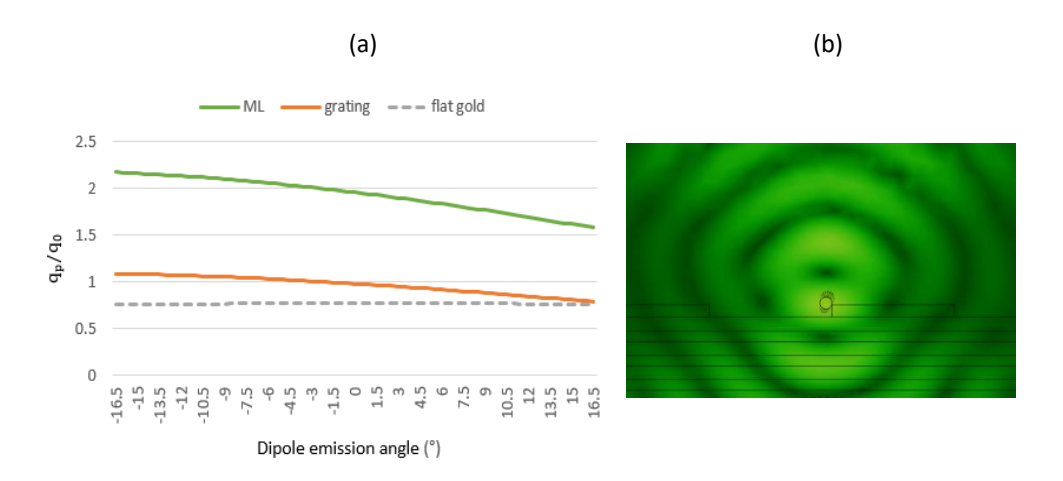


Fig. 30. a) The comparison chart of UC enhancement ratio showcasing the effect of adding multilayers to the grating for the emission. b) Dipole emission at the position P_4 with emission angle of -16.5° and wavelength of 540 nm.

Since UC measurement is missed from our work due to time limitation, we cannot present an experimental value for UC enhancement factor as we needed the averaged emission intensity ratio to the flat gold as reference. Nevertheless, considering the same quenching effect for flat gold and the relationship between simulated QY enhancement, we can guess that the total enhancement factor with ML structure is doubled and can be around 130-fold enhancement. In comparison with the last plasmonic grating structure, our new design with multilayers can be applied for increasing emission enhancement of various biosensing applications due to directionality and excitation wavelength selectivity.

In the future studies, to have a true high up-conversion enhancement, we can consider designing a dielectric meta-surface on the multilayers with greater PBG performance on reflecting emission wavelength, which will also give Mie resonance, Fano resonance and hopefully, a better emission. In addition to continuous-wave operation, time-resolved measurements for pulse operation and the UCNP emission spectrum are suggested for further experimental investigation, which will require a slight modification to the previous setup to allow upward transmission (exciting SPPs from substrate).

References

- [1] Schuler, Benjamin, and Hagen Hofmann. "Single-molecule spectroscopy of protein folding dynamics—expanding scope and timescales." Current opinion in structural biology 23, no. 1 (2013): 36-47.
- [2] Taylor, Adam B., and Peter Zijlstra. "Single-molecule plasmon sensing: current status and future prospects." ACS sensors 2, no. 8 (2017): 1103-1122.
- [3] Zijlstra, P., Paulo, P. & Orrit, M. Optical detection of single non-absorbing molecules using the surface plasmon resonance of a gold nanorod. Nature Nanotech 7, 379–382 (2012).
- [4] R Hutter, Eliza, and Janos H. Fendler. "Exploitation of localized surface plasmon resonance." Advanced materials 16, no. 19 (2004): 1685-1706.
- [5] issin, D. M. et al. (2010). Single-molecule enzyme-linked immunosorbent assay detects serum proteins at subfemtomolar concentrations. Nature Biotechnology, 28(6), 595–599.
- [6] Mayer, K. M., & Hafner, J. H. (2011). Localized surface plasmon resonance sensors. Chemical Reviews, 111(6), 3828–3857.
- [7] Punj, D., et al. (2017). Plasmonic antennas and zero-mode waveguides to enhance single-molecule fluorescence detection and fluorescence correlation spectroscopy toward physiological concentrations. WIREs Nanomedicine and Nanobiotechnology, 9(4), e1444.
- [8] Takaloo, S.; Xu, A.H.; Zaidan, L.; Irannejad, M.; Yavuz, M. Towards Point-of-Care Single Biomolecule Detection Using Next Generation Portable Nanoplasmonic Biosensors: A Review. Biosensors 2024, 14, 593. https://doi.org/10.3390/bios14120593.
- [9] S. A. Hilderbrand, F. Shao, C. Salthouse, U. Mahmood, and R. Weissleder, "Upconverting luminescentnanomaterials: Application to in vivo bioimaging," Chemical Communications, no. 28, pp. 4188–4190, 2009, doi: 10.1039/b905927j.
- [10] S. Xu, S. Huang, Q. He, and L. Wang, "Upconversion nanophosphores for bioimaging," TrAC Trends in Analytical Chemistry, vol. 66. Elsevier B.V., pp. 72–79, Mar. 01, 2015. doi: 10.1016/j.trac.2014.11.014.
- [11] M. v. DaCosta, S. Doughan, Y. Han, and U. J. Krull, "Lanthanide upconversion nanoparticles and applications in bioassays and bioimaging: A review," Analytica Chimica Acta, vol. 832. Elsevier, pp. 1–33, Jun. 17, 2014. doi: 10.1016/j.aca.2014.04.030.
- [12] Auzel, F. (2004). Upconversion and anti-Stokes processes with f and d ions in solids. Chemical Reviews, 104(1), 139–174.
- [13] Wang, F., & Liu, X. (2009). Recent advances in the chemistry of

- lanthanide-doped upconversion nanocrystals. Chemical Society Reviews, 38(4), 976–989.
- [14] G. R. Tan, M. Wang, C. Y. Hsu, N. Chen, and Y. Zhang, "Small Upconverting Fluorescent Nanoparticles for Biosensing and Bioimaging," Advanced Optical Materials, vol. 4, no. 7, pp. 984–997, Jul. 2016, doi:10.1002/adom.201600141.
- [15] F. T. Rabouw, P. T. Prins, P. Villanueva-Delgado, M. Castelijns, R. G. Geitenbeek, and A. Meijerink, "Quenching Pathways in NaYF4:Er3+,Yb3+ Upconversion Nanocrystals," ACS Nano, vol. 12, no. 5, pp. 4812–4823, May 2018, doi: https://doi.org/10.1021/acsnano.8b01545.
- [16] Das, A., Mao, C., Cho, S. et al. Over 1000-fold enhancement of upconversion luminescence using water-dispersible metal-insulator-metal nanostructures. Nat Commun 9, 4828 (2018).
- [17] Le, Duc, Kreivi, Marjut, Aikio, Sanna, Heinilehto, Noora, Sipola, Teemu, Petäjä, Jarno, Guo, Tian-Long, Roussey, Matthieu and Hiltunen, Jussi. "Surface plasmon polariton-enhanced upconversion luminescence for biosensing applications" Nanophotonics, vol. 13, no. 21, 2024, pp. 3995-4006.
- [18] Bhaskar, S.; Das, P.; Moronshing, M.; Rai, A.; Subramaniam, C.; Bhaktha, S. B.; Ramamurthy, S. S. Photoplasmonic assembly of dielectric-metal, Nd2O3-Gold soret nanointerfaces for dequenching the luminophore emission. Nanophotonics 2021, 10, 3417–3431.
- [19] Yaltaye, Mulusew Wondie. "Curved Multilayered Structure for Directional Raman Enhancement." Master's thesis, Itä-Suomen yliopisto, 2022.
- [20] Xiong, Yanyu, Skye Shepherd, Joseph Tibbs, Amanda Bacon, Weinan Liu, Lucas D. Akin, Takhmina Ayupova, Seemesh Bhaskar, and Brian T. Cunningham. "Photonic crystal enhanced fluorescence: a review on design strategies and applications." Micromachines 14, no. 3 (2023): 668.
- [21] Bhaskar, S.; Lis, S. M.; Kanvah, S.; Bhaktha, B. N. S.; Ramamurthy, S. S. Single-Molecule Cholesterol Sensing by Integrating Silver Nanowire Propagating Plasmons and Graphene Oxide π -Plasmons on a Photonic Crystal-Coupled Emission Platform. ACS Appl. Opt. Mater. 2023, **1** (1), 159–172. https://doi.org/10.1021/acsaom.2c00026.
- [22] Bhaskar, S. et al. (2022). Materials Research, 56(7), 1025-1036
- [23] Paternò GM, Moscardi L, Donini S, Ariodanti D, Kriegel I, Zani M, Parisini E, Scotognella F, Lanzani G. Hybrid One-Dimensional Plasmonic-Photonic Crystals for Optical Detection of Bacterial Contaminants. J Phys Chem Lett. 2019 Sep 5;10(17):4980-4986. doi: 10.1021/acs.jpclett.9b01612. Epub 2019 Aug 15. PMID: 31407906.

- [24] Liu, J.-N., Huang, Q., Liu, K.-K., Singamaneni, S., & Cunningham, B. T. (2017). Nanoantenna–Microcavity Hybrids with Highly Cooperative Plasmonic–Photonic Coupling. arXiv preprint arXiv:1704.07867.
- [25] Hajshahvaladi L, Kaatuzian H, Moghaddasi M, Danaie M. Hybridization of surface plasmons and photonic crystal resonators for high-sensitivity and high-resolution sensing applications. Sci Rep. 2022 Dec 9;12(1):21292. doi: 10.1038/s41598-022-25980-y. PMID: 36494440; PMCID: PMC9734182.
- [26] Krupin, O., & Berini, P. (2019). Long-Range Surface Plasmon-Polariton Waveguide Biosensors for Human Cardiac Troponin I Detection. Sensors, 19(3), 631.
- [27] Boltasseva, Alexandra & Søndergaard, Thomas & Nikolajsen, Thomas & Leosson, Kristjan & Bozhevolnyi, Sergey & Hvam, J.. (2005). Propagation of long-range surface plasmon polaritons in photonic crystals. Journal of the Optical Society of America B. 22. 2027-2038. 10.1364/JOSAB.22.002027.
- [28] Hasan, M. R., Akter, S., Rifat, A. A., Rana, S., & Ali, S. (2017). A Highly Sensitive Gold-Coated Photonic Crystal Fiber Biosensor Based on Surface Plasmon Resonance. Photonics, 4(1), 18.
- [29] Getahun Kumela, Alemayehu & Gemta, Abebe & Kebede, Alemu & Haileselasse, Ruth & Mekonnen, Habtamu Dagnaw & Yasin, Umer & Woldegiorges, Kinfe. (2023). A Review on Hybridization of Plasmonic and Photonic Crystal Biosensors for Effective Cancer cell Diagnosis. 10.1039/D3NA00541K.
- [30] Haase, M., & Schäfer, H. (2011). Upconverting nanoparticles. Angewandte Chemie International Edition, 50(26), 5808–5829.
- [31] Chen, G., Qiu, H., Prasad, P. N., & Chen, X. (2014). Upconversion nanoparticles: Design, nanochemistry, and applications in theranostics. Chemical Reviews, 114(10), 5161–5214.
- [32] Wang, F., & Liu, X. (2009). Recent advances in the chemistry of lanthanide-doped upconversion nanocrystals. Chemical Society Reviews, 38(4), 976–989.
- [33] Wilhelm, Stefan. "Perspectives for upconverting nanoparticles." ACS nano 11, no. 11 (2017): 10644-10653.
- [34] Wu, S., Butt, H. J., & Chu, Z. (2022). Near-infrared excitation of upconversion nanoparticles for bioimaging. Advanced Optical Materials, 10(2), 2101123.
- [35] Dong, H., Sun, L. D., & Yan, C. H. (2015). Energy transfer in lanthanide upconversion studies for extended optical applications. Chemical Society Reviews, 44(6), 1608–1634.
- [36] Heer, S., Kömpe, K., Güdel, H. U., & Haase, M. (2004). Highly efficient multicolour upconversion emission in transparent colloids of

- lanthanide-doped NaYF₄ nanocrystals. Advanced Materials, 16(23–24), 2102–2105.
- [37] Burikov, S.; Filippova, E.; Proydakova, V.; Kuznetsov, S.; Voronov, V.; Tabachkova, N.; Dolenko, T. The Influence of Concentrations of Sensitizers and Activators on Luminescence Kinetics Parameters of Up-Conversion Nanocomplexes NaYF4:Yb3+/Tm3+. Photonics 2024, 11, 228.
- [38] Liu, X., Liu, L., Zhao, J., Chen, X., & Liu, Y. (2015). Phonon-assisted energy back transfer-induced multicolor upconversion emission of Gd_2O_3 :Yb³+/Er³+ nanoparticles under near-infrared excitation. Physical Chemistry Chemical Physics, 17(25), 16670–16677.
- [39] Chen, X., Peng, D., Ju, Q., & Wang, F. (2014). Photon upconversion in core–shell nanoparticles. Chemical Society Reviews, 43(10), 3205–3221.
- [40] Zhou, B., Shi, B., Jin, D., & Liu, X. (2015). Controlling upconversion nanocrystals for emerging applications. Nature Nanotechnology, 10(11), 924–936.
- [41] Zhang, J., et al. (2012). Surface plasmon polaritons: physics and applications. Journal of Physics D: Applied Physics, 45(11), 113001.
- [42] H. Raether, Surface Plasmons on Smooth and Rough Surfaces and on Gratings. Springer, 1998.
- [43] Fitzpatrick, Richard. Waveguide Modes. University of Texas at Austin, https://farside.ph.utexas.edu/teaching/316/lectures/node128.html. (Accessed 2007-07-14).
- [44] Kumar, G., Sarswat, P.K. (2016). Interaction of Surface Plasmon Polaritons with Nanomaterials. In: Geddes, C. (eds) Reviews in Plasmonics 2015. Reviews in Plasmonics, vol 2015. Springer, Cham. https://doi.org/10.1007/978-3-319-24606-2_5.
- [45] Zayats, Anatoly V., Igor I. Smolyaninov, and Alexei A. Maradudin. "Nano-Optics of Surface Plasmon Polaritons." Physics Reports 408, no. 3–4 (March 2005): 131–314.
- [46] D. M. Wu, A. García-Etxarri, A. Salleo, and J. A. Dionne, "Plasmon-Enhanced Upconversion," Journal of Physical Chemistry Letters, vol. 5, no. 22, pp. 4020–4031, Nov. 2014, doi: https://doi.org/10.1021/jz5019042.
- [47] Barnes, William L. "Surface plasmon—polariton length scales: a route to sub-wavelength optics." Journal of optics A: pure and applied optics 8, no. 4 (2006): S87.
- [48] Lidorikis, Elefterios, Qiming Li, and Costas M. Soukoulis. "Wave Propagation in Nonlinear Multilayer Structures." Physical Review B 54, no. 15 (October 1996): 10249–10252. https://doi.org/10.1103/PhysRevB.54.10249.

- [49] Moussa, Romany, Laurent Salomon, Pierre-Jean Dufour, and Hafid Aourag. "Large Photonic Band Gap in One Dimension Multilayer Structure." Journal of Physics and Chemistry of Solids 63, no. 5 (May 2002): 725–732. https://doi.org/10.1016/S0022-3697(01)00221-9.
- [50] Karlene Rosera Maskaly, Garry R. Maskaly, W. Craig Carter, and James L. Maxwell, "Diminished normal reflectivity of one-dimensional photonic crystals due to dielectric interfacial roughness," Opt. Lett. 29, 2791-2793 (2004).
- [51] Krauss, TF., DeLaRue, RM., & Brand, S. (1996). Two-dimensional photonic-bandgap structures operating at near infrared wavelengths. Nature, 383(6602), 699-702.
- [52] Labilloy, D. et al. (1999). Measuring the optical properties of twodimensional photonic crystals in the near infrared. In: Benisty, H., Weisbuch, C., Polytechnique, É., Gérard, JM., Houdré, R., Rarity, J. (eds) Confined Photon Systems. Lecture Notes in Physics, vol 531. Springer, Berlin, Heidelberg.
- [53] Johnson, Steven G., Shanhui Fan, Pierre R. Villeneuve, J. D. Joannopoulos, and L. A. Kolodziejski. "Guided Modes in Photonic Crystal Slabs." Physical Review B 60, no. 8 (1999): 5751–5758.
- [54] Özbay E, Abeyta A, Tuttle G, Tringides M, Biswas R, Chan CT, Soukoulis CM, Ho KM. Measurement of a three-dimensional photonic band gap in a crystal structure made of dielectric rods. Phys Rev B Condens Matter. 1994 Jul 15;50(3):1945-1948. doi: 10.1103/physrevb.50.1945. PMID: 9976387.
- [55] Inoue, Si. (2013). Photonic Crystals: Manipulating Light with Periodic Structures. In: Aoyagi, Y., Kajikawa, K. (eds) Optical Properties of Advanced Materials. Springer Series in Materials Science, vol 168. Springer, Berlin, Heidelberg.
- [56] Kuramochi, E., Notomi, M., Kawashima, T. et al. A new fabrication technique for photonic crystals: Nanolithography combined with alternating-layer deposition. Optical and Quantum Electronics 34, 53–61 (2002).
- [57] Joannopoulos, J. D., R. D. Meade, and I. N. Winn. Photonic Crystals: Molding the Flow of Light. Princeton, NJ: Princeton University Press, 1995.
- [58] Armstrong, Eileen, and Colm O'Dwyer. "Artificial opal photonic crystals and inverse opal structures—fundamentals and applications from optics to energy storage." *Journal of materials chemistry C* 3, no. 24 (2015): 6109-6143.
- [59] Charles Kittel, Introduction to Solid State Physics (New York: John Wiley & Sons, 1976).
- [60] Vijay Koju and William M. Robertson, "Excitation of Bloch-like surface

- waves in quasi-crystals and aperiodic dielectric multilayers," Opt. Lett. 41, 2915-2918 (2016).
- [61] Orfanidis, Sophocles J. Electromagnetic Waves and Antennas. Piscataway, NJ: Rutgers University, 2002.
- [62] Wave Optics Module," Comsol Multiphysics. Accessed: May 05, 2022. [Online]. Available:
- [63] A. D. Rakic, A. B. Djuris, J. M. Elazar, and M. L. Majewski, "Optical properties of metallic films for vertical-cavity optoelectronic devices Aleksandar," Applied Optics, vol. 37, no. 22, pp. 5271–5283, 1998.
- [64] Brzozowska, M., & Hildebrandt, N. (2023). Plasmonic quenching and enhancement: metal—quantum dot nanohybrids for fluorescence biosensing. Chemical Communications.

Appendix

Appendix A. Abbreviations

UC Upconversion

SPPs Surface plasmon polaritons

NIR Near-infrared

1D PhCs One-dimentional Photonic crystals

ML Multilayer

UCNPs Upconversion nanoparticles

PBG Photonic band gap

FEM Finite element method

TMM Transfer matrix method

TM Transverse magnetic

TE Transverse electric

EBL Electron beam lithography

ALD Atomic layer deposition

SEM Scanning electron microscopy

GPC Growth per cycle

EF Enhancement factor

QY Quantum yield

Statement of non-plagiarism

"I hereby declare that all information in this report has been obtained and presented in accordance with academic rules and ethical conduct and the work I am submitting in this report, except where I have indicated, is my own work."

Statement of AI tools usage

I hereby declare that generative AI tools, including large language models (e.g., ChatGPT), were employed in the preparation of this thesis solely for ancillary purposes such as improving clarity of expression, assisting in the refinement of language, and providing structural suggestions. The substantive intellectual contributions, including research design, data analysis, simulations, interpretation, and conclusions, are entirely my own and I critically reviewed and edited all AI-generated text.

Date and signature of the author

25/08/2025

Supervisor approval

I, the undersigned, **Matthieu Roussey**, supervisor of **Ayda Nasiri**, student of the PSRS EMJMD, during her master thesis at the University of Eastern Finland certify that I approve the content of this master thesis report entitled "Synergy of Surface Plasmon Polaritons and Photonic Crystals for Enhanced Emission in Biosensing Application".

Date and signature of the supervisor

20/08/2025